Structural and Geomorphic Mapping of Northern Claritas Fossae and the Thaumasia Graben, Mars: Implications for Formation

by

Genevieve Lynn Studer-Ellis

A Thesis Presented in Partial Fulfillment
of the Requirements for the Degree
Master of Science

Approved July 2019 by the
Graduate Supervisory Committee:

David Williams, Co-Chair
Philip Christensen, Co-Chair
Ramon Arrowsmith

ARIZONA STATE UNIVERSITY

August 2019

ABSTRACT

In this thesis, I investigate possible formation processes in the northern Claritas Fossae and the large Thaumasia graben on Mars. In particular, I assess three proposed formation hypotheses for the region: a mega-landslide across the Thaumasia plateau, originating in Tharsis and moving to the south-west; a rift system pulling apart Claritas Fossae and opening the large Thaumasia graben generally propagating in a north-south direction: and extension caused by uplifting from underlying dike swarms. Using digital terrain models (DTMs) from the High Resolution Stereo Camera (HRSC) aboard Mars Express and visual images from the Context Camera (CTX) aboard the Mars Reconnaissance Orbiter (MRO), I analyzed the geomorphic and structural context of the region. Specifically, I produced geomorphologic and structural feature maps, conducted sector diagram analyses of fault propagation direction, calculated and compared extension and strain in local and regional samples, analyzed along strike throw-profiles of faults, and conducted surface age estimates through crater counting. I found that no single formation mechanism fully explains the surface features seen in Northern Claritas Fossae today. Instead I, propose the following sequence of events led to the surface characteristics we now observe. The region most likely underwent two episodes of uplift and extension due to sub-surface magmatic intrusions, then experienced an extensional event which produced the large Thaumasia graben. This was followed by the emplacement of a layer of lava burying the bottom of the Thaumasia graben and the eastern edge of the region. Additional extension followed across the eastern portion of the study area, and finally of a young lava flow was emplaced abutting and overprinting the southwestern edge.

DEDICATION

To my grandmother Rita Ellis

You gave birth to a legacy of strong women;

I wish that you could have been here to see me accomplish this.

To all the women, girls, and LGBTQIA+ individuals thinking about the world, planets, and stars; may you find the path you are meant to walk.

ACKNOWLEDGMENTS

I would like to acknowledge and thank my committee for their assistance throughout the life of this project. First Dr. David Williams, who welcomed me when I showed up outside his door with only a vague idea of what I wanted to do. He inspired me to delve deep into literature and keep refining my question until I had the makings of a robust project. He always provided guidance when I needed it, while always allowing the project to remain my own. Next to Dr. Phil Christensen, who pushed me to reconsider ideas I had previously discarded to the betterment of this project. Finally, to Dr. Ramon Arrowsmith, who provided guidance on all things structural and encouraged me to expand my structural analysis wheelhouse.

To the staff of the Ronald Greeley Center for Planetary Studies: A National Aeronautics and Space Administration (NASA), Regional Planetary Image Facility (RPIF) at Arizona State University (ASU), thank you for letting me use the facility at all hours, especially when I became a night owl/ghost. Especially to David Nelson for his assistance in all things technical including, but not limited to: ArcGIS™, selecting an external hard drive, and keeping all of the software in the RPIF up to date. David also provided an invaluable sounding board whenever I ran into a problem and allowed me to work my own way through them by asking me question after question. To Amy Zink who was always available for a consultation on the nuances of color choices, bouncing ideas off of, and supportive encouragement, thank you very much.

I would like to acknowledge all of the specialized software and technical resources I utilized in my project. Maps throughout this thesis were created using ArcGIS® software by Esri®. ArcGIS and ArcMap™ are the intellectual property of Esri

and are used here under license. Copyright © Esri. All rights reserved. For more information about Esri software please visit www.esri.com. Maps were also created using Java Mission-planning and Analysis for Remote Sensing (JMARS) software. JMARS was developed by ASU's Mars Space Flight Facility and more information about JMARS can be found at www.jmars.mars.asu.edu. This research has made use of the United States Geological Survey (USGS) Integrated Software for Imagers and Spectrometers (ISIS) version 3 as well as the USGS and NASA's Planetary Data System (PDS).

To my many friends who have provided invaluable support and encouragement through these long years, thank you. To Dr. Jessica Noviello, we will always have that family Italian restaurant for eating endless bowls of pasta. To Zaellotius Wilson, I will always appreciate the abdominal workout that results from the raucous bouts of laughter every time we're together. To Lena Heffern, thank you for pushing me to go for what I want. To Lucia Perez, your arepas are the best I've ever had, and you are a star pottery painting partner.

To my family who have picked me up when I've been knocked down, who have only ever wished the best for me, I love you to Mars and back. A special mention to the woman who may not share my blood but couldn't be better sisters to me: Sierra Ferguson and Alyssa Sherry. The two of you have held me when I cried, picked me up, dusted me off, and catapulted me onto bigger and better things. To my rock, my always there for a midnight phone call, my "I don't care if you don't want my help, you're getting it anyway," also known as my mother. There are no words, only love. To my editor in chief, my d-man, "put on sunscreen" reminder, also known as my dad, you are a GdNdFdCd and FHF.

TABLE OF CONTENTS

Page

LIST OF TABLES

LIST OF FIGURES

Figure Page

CHAPTER 1

INTRODUCTION

Early planetary evolution and structural dynamics are poorly understood for both Mars and Earth. Earth has undergone crustal recycling because of plate tectonics and therefore there are few samples of significant age (>1 Ga) exist on Earth. The portions of Earth which are of significant age are generally located in the interior of continents as cratons. Those rocks have undergone considerable alteration throughout their lives and the surfaces of the cratons have also undergone considerable alteration. Therefore, studying early planetary dynamics (structural and volcanic evolution in particular) on Earth is challenging at best.

Mars, however, can be used as a space-for-time substitution because of its mono-plate structure and lack of crustal recycling. Ancient areas of Mars, including Thaumasia, are frequently used to study the evolution of crustal dynamics (volcanic, structural deformation and evolution at surface).

The region of Thaumasia, Mars is a geomorphologically diverse area containing highland and lowland terrains (planum, terra, and fossae) modified by varying degrees of cratering that indicate different ages (J. M. Dohm et al., 2001; Dohm and Tanaka, 1999; Tanaka et al., 2014) . Figure 1 shows the extent of the region in reference to a global view of Mars. The Thaumasia region extends across a large (~60° E/W by 35° N/S) portion of the Martian surface, from just southeast of the Tharsis Volcanic province, to the edge of Vallis Marineris in the east, and south to Aonia Terra. The ages of features inside Thaumasia range from the early Noachian (4.1 Ga to 3.7 Ga) through the Hesperian (3.7 Ga to 3 Ga) and Amazonian (3 Ga to present) (J. M. Dohm et al., 2001;

Tanaka et al., 2014). Major regions in Thaumasia include (but are not limited to) the Thaumasia Planum, Thaumasia Highlands, Claritas Fossae and Solis Planum.

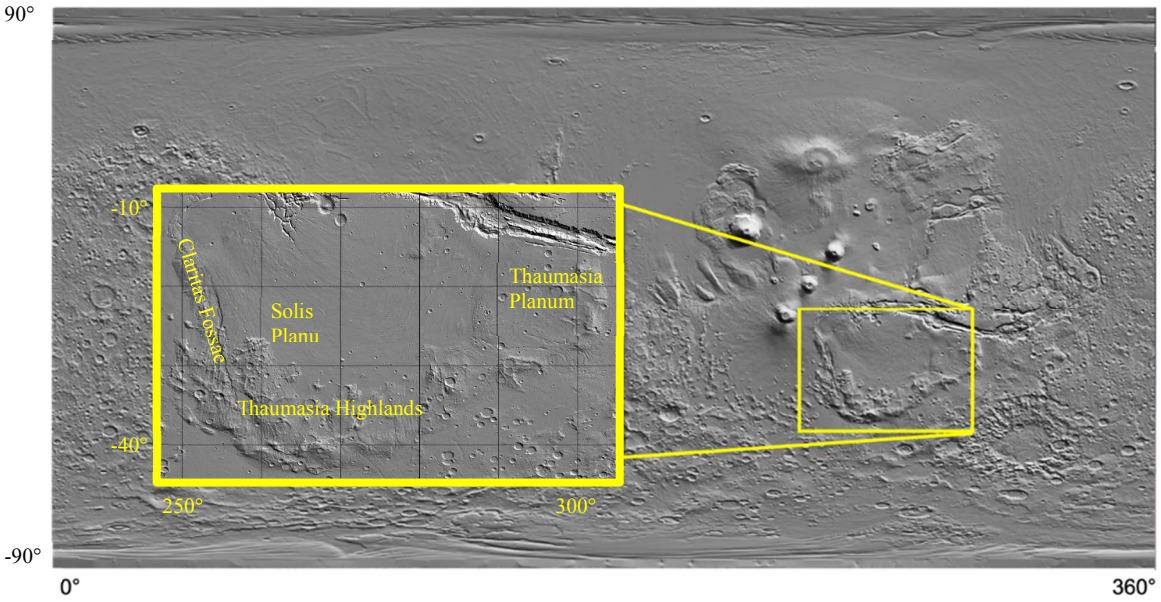

Figure 1: Location map of study area in Thaumasia. Northern Claritas Fossae is the location of the region of interest. Basemap shown is the MOLA shaded relief. Figure was produced using JMARS™ (Christensen et al., 2009).

The Thaumasia Highlands are a mountain range which extend across the Thaumasia region from 250° to 300° E, and 15° to 45° S (Figure 1). The northern portion of Claritas Fossae, located on the western flank of the Thaumasia Highlands, is where I have focused my study. Northern Claritas Fossae has an average elevation in the 6-8 km above the Martian aroid (Figure 2). Claritas Fossae is covered in lineations interpreted as graben sets and normal faults (predominately NS-trending), including a long NS-trending graben sometimes referred to as the Thaumasia graben (Dohm and Tanaka, 1999; Hauber and Kronberg, 2005).

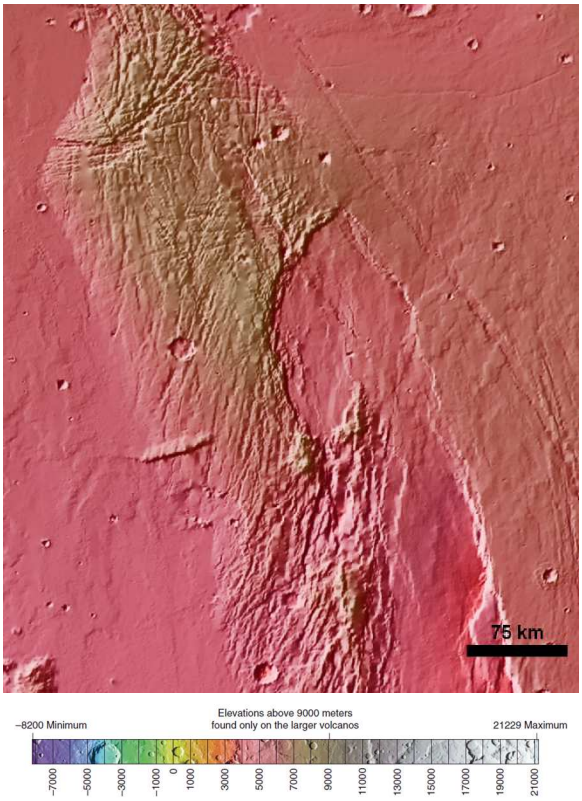

Figure 2: MOLA shaded relief of Northern Claritas Fossae. Elevation ranges from ~5500 to 7900 meters.

Because Thaumasia contains a diverse extent of surfaces developed over a significantly large portion of the Martian timescale the region is of the utmost interest to scientists. The region has been heavily studied throughout the years with a quadrangle map of the region produced by (James M Dohm et al., 2001). Dohm et al., used techniques developed to investigate the structural and stratigraphic history of planetary surfaces. Their map, in three parts "geologic, paleotectonic, and paleoerosional," shows a complex region with a diverse geologic, structural, and volcanic history. Dohm et al., (2001) conclude that there were five stages of region formation. In each stage distinct structural deformation occurs. Additionally, there are two main construct-forming

volcanic periods (Noachian-Hesperian and Amazonian) Of particular interest are the structural regimes which Dohm et al., 2001 couple with volcanic production suggesting a link between tectonic and magmatic processes in the region. Therefore, understanding the region's development can provide important insights into the history of Mars itself.

Dohm and Tanaka (1999) interpret the Thaumasia Highlands as an early Noachian tectonic mountain building site and as a source for channel systems. The production of the volcanic material in the highlands is thought to have occurred via repeated volcanic episodes with modification by tectonism after volcanic emplacement (Hood et al., 2016). Structural and tectonic formation mechanisms for the Thaumasia highlands and Thaumasia region at large have been proposed by Dohm et al. (1999), Williams et al. (2008), and Grott et al. (2007). Mechanisms proposed by those studies suggest that the region formed by volcanic emplacement and was later deformed by extensional processes such as stress induced extension because of Tharsis uplift, and crustal flexure caused by underlying heat flux.

Chemical composition has been examined to further understand the aforementioned possible formation mechanisms. The greater Thaumasia region has chemical signatures from volcanic episodes consistent with a magmatic evolution of basalt in three distinct provinces (Hood et al., 2016). Hood et al. (2016) used remotely sensed surface chemistry through data acquired by the Mars Odyssey Gamma Ray Spectrometer. The first province near Syria Planum is depleted in K and Th, the second in Solis Planum is enriched in Si but depleted in H, K, and Th, the final province which spans the majority of Thaumasia Planum is enriched in Si and depleted in H. Note that the western flanks of Thaumasia, including Claritas Fossae are covered in the ubiquitous

Martian “dust” and are therefore lacking in spectral observations. These provinces were found to be inconsistent with a proposed mega-landslide origin for the region, since there is a distinct lack of salt deposit signatures across the region. However, the provinces are consistent with distinct magmatic emplacements of differing compositions, all of a basaltic composition and enriched in Si, lending credence to the proposed mechanisms of either an early rift system or sub surface dike swarms.

Other studies suggest that the highlands in the region formed because of lithospheric flexure during sub-surface volcanic melt emplacement (Anguita et al., 2006; Nahm and Schultz, 2010). Additional explanations for the formation of the Thaumasia highlands include large-scale or mega-landslide caused by a salt failure plane initiated by uplifting from the Tharsis complex (Andrews-Hanna, 2009; Montgomery et al., 2009; Montgomery and Gillespie, 2005), uplift through early plate tectonics and rift zone production (Hauber and Kronberg, 2005), and extension and uplift caused by underlying dike swarm emplacement (Ernst, Grosfils, and Mège 2001).

This study refines the possible formation mechanisms for the Thaumasia graben and northern Claritas Fossae. Not every formation mechanism listed is addressed in this study. Table 1 summarizes the formation mechanisms, main features of the mechanisms, and who proposed the mechanisms that this study will address. Individual mechanisms reviewed in this study are discussed in further detail here

Table 1: Summary of possible formation mechanisms for the region of interest (ROI) and key features for each mechanism.

Formation Mechanism	Key Features
Mega-landslide*	Rolling Lobate Surface Across Flow Lobate Edge to Flow with Margin Toe Scarp Detachment at Origin Faults Parallel to Flow Front
Rift System**	Regional and Locally Uniform Extension Faulting in Parallel and En Echelon Patterns Faulting in Triple Junction Morphology
Underlying Dike Swarm***	Grabens in radiating, circumferential and or subparallel patterns Pit Craters and Ovoid/Linear Troughs Spatter Cones and other volcanics Exhumed Dike Outcrops in Graben Centers

*Montgomery 2009, and Andrews-Hanna 2009
**Hauber and Kronberg 2005
***Ernst, Grosfils, and Mège 2001

The Thaumasia region is proposed by Montgomery et al., (2005), Montgomery et al., (2009) and Andrews-Hannah (2009) to have formed from a mega-landslide originating from the NW and flowing to the SE in (Figure 2). They posit that the intrusion of the Tharsis volcanic complex led to an uplifting of the NW region and sufficient topographic slope and regional heat flux to activate a failure plane composed of sub-surface ice aquifer loaded with "discontinuous weak layers of impure salts and ice" and allow gravitationally directed slumping in a SE direction to occur. This would produce a long flow front slide with multiple wrinkle ridges parallel to the flow front and ending in a toe of compressed material SE of Tharsis. The study compares the Thaumasia region with Whiting Dome in the Gulf of Mexico as a smaller scale terrestrial analog.

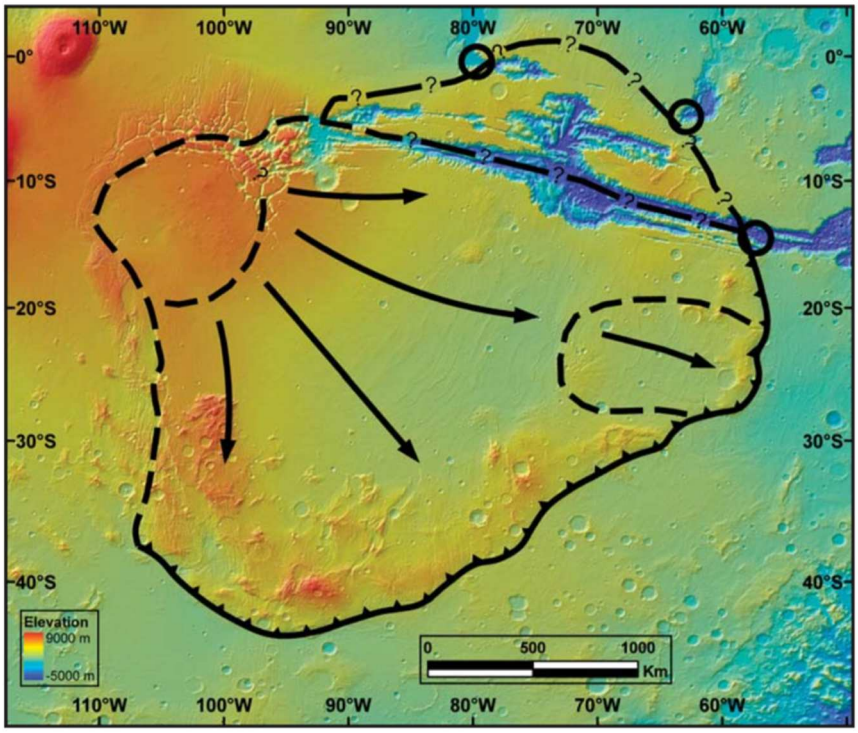

Figure 3: Colorized "shaded-relief [elevation] map of the Thaumasia Plateau (Thermal Emission Imaging System infrared (THEMIS IR) base) showing the broad-scale, inferred sense of translation during gravity spreading, and the boundaries of 'microplates' (dashed lines) and outflow channels (open circles)." from Montgomery et al., 2009.

In contrast, the Thaumasia graben and the Kenya Rift system are compared using regional extension analysis and geomorphological studies by Hauber and Kronberg (2005). They compare possible Martian rift systems to the Kenya Rift in East Africa: Figure 4 visually compares the Thaumasia graben, the Kenya Rift, and Tempe Fossae, Mars. Tempe Fossae, Mars and the Kenya Rift are compared by Hauber and Kronberg (2001). They conclude that Thaumasia graben has some characteristics consistent with the Kenya Rift system but lacks four key features, namely "regional domal uplift, the formation of a through-going rift valley, a flank uplift, and rift-related volcanism" (Hauber and Kronberg, 2005).

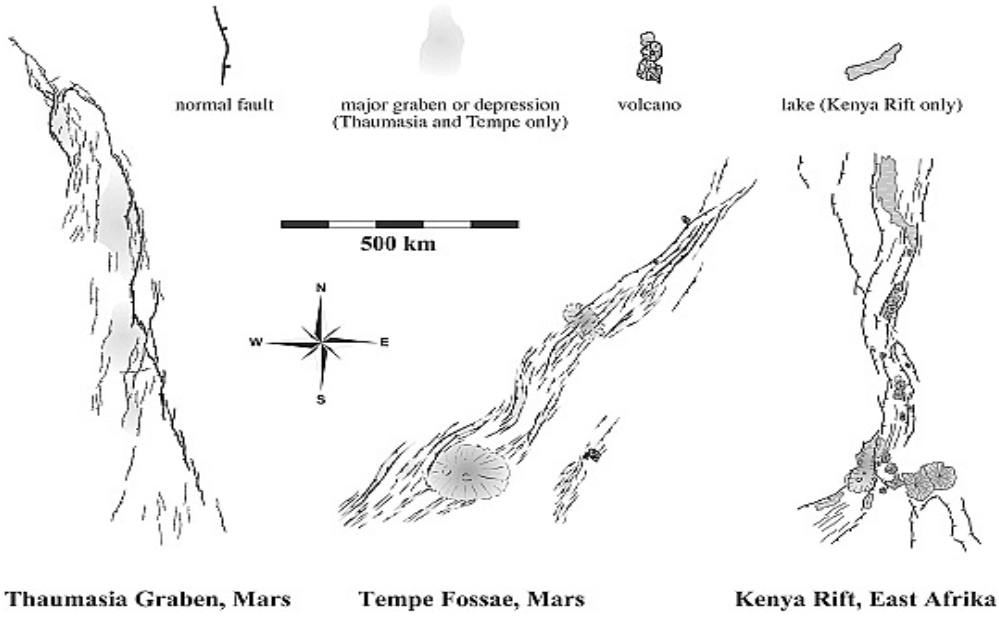

Figure 4: Same scale comparison of the Thaumasia graben, Mars, Tempe Fossae, Mars and the Kenya Rift, East Africa Earth. "Note the overall similarity in gross dimensions." Figure is adapted from Hauber and Kronberg (2005).

Finally, the regions of Claritas Fossae and Syria Planum, Mars are interpreted as surface extensional expressions of sub-surface dike swarms by Ernst et al. (2002). They estimate that there are convergence centers of dike swarms in Syria Planum, and in the middle of Claritas Fossae, both of which are contributing to the extension seen in my study area. They describe how a magma intrusion at depth can produce graben sets at the surface in six primary patterns, illustrated in Figure 5. They detail geomorphic evidence for dike swarms as graben sets in one of the six patterns co-occurring with volcanic features (such as "pit craters, ovoid and linear troughs, shallow ovoid flat-floored depressions, and spatter cones," Ernst et al., 2001). They also discuss how intrusions of dike swarms can produce surface features similar to yet distinct from volcanic rifting. In particular, volcanic rifting can produce surface collapse after reservoir withdrawal. It is important to note that volcanic rifting can be accompanied by dike intrusion and dilation at depth between the reservoir and stretched surface. Therefore, dikes cannot always be counted as a primary source of extension; sometimes they are secondary to volcanic rifting.

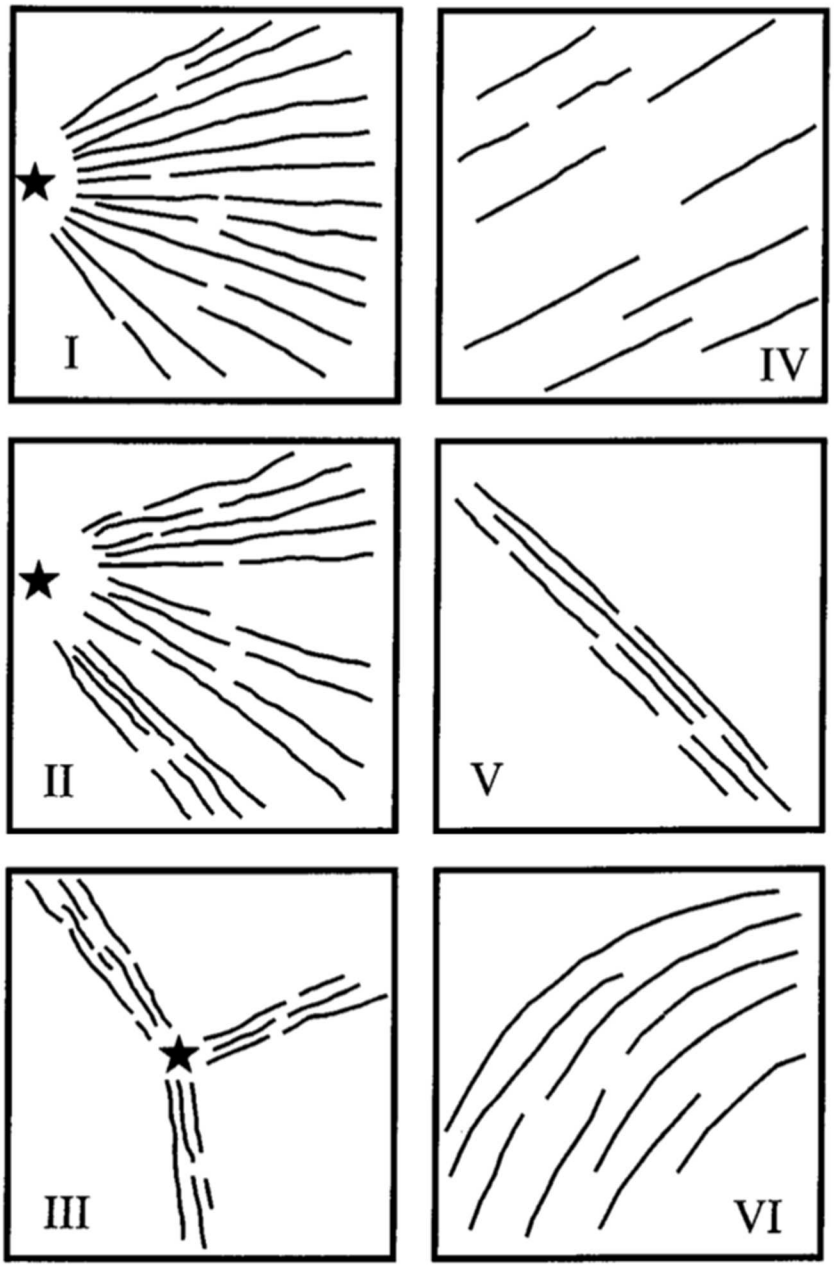

Figure 5: "Six characteristic geometries of giant radiating dike swarms…I = continuous fanning pattern; II = fanning pattern subdivided into separate subswarms; III = subswarms of subparallel dikes that radiate from a common point; IV = subparallel dikes over a broad area; V = subparallel dikes in a narrow zone; VI = arcuate pattern. Stars locate probable mantle plume center defined by convergence of radiating dike patterns." From Ernst et al., (2001).

The complex topography of the area suggests an intricate structural history which is best investigated through a combination of visual and elevation-based analyses.

New higher resolution data from the Context Imager (CTX) and the High Resolution Stereo Camera (HRSC) data aboard the Mars Reconnaissance Orbiter (MRO) and Mars Express orbiter, respectively, enable image and structural analysis on a much finer scale than has been previously available. Using data from the aforementioned missions, my project analyzes the Thaumasia graben extensional regime through mapping and structural analysis. Specifically, this project produces a geomorphic map, a structural feature map, an analysis of fault propagation direction through sector diagram analysis, an analysis of extension and strain, an analysis of along strike slip profiles, and some limited crater counting for age analysis. This study will compare the data generated through the previously mentioned analysis to the proposed data patterns of the formation mechanisms listed in Table 1 to refine possible formation mechanisms for the region (Thaumasia) and local geomorphology (Claritas Fossae).

CHAPTER 2

METHODS

2.1 OVERVIEW

To refine possible formation mechanisms for the Thaumasia graben, northern Claritas Fossae, and Thaumasia, this study used various pieces of software for mapping and image processing. These included ArcGIS™ (ESRI) and United States Geological Survey (USGS) Integrated Software for Imagers and Spectrometers Version 3 (ISIS3) (Anderson and Sides, 2004) to process images in the region of interest (ROI). Within the following sections, I summarize 1) data acquisition, 2) image calibration, 3) geomorphological map production and structural analysis, and 4) crater age analysis.

2.2 AQUIRING DATA

Data were selected from images taken by the High Resolution Stereo Camera (HRSC) and Context Imager (CTX) instruments aboard the Mars Express and the Mars Reconnaissance Orbiter (MRO) spacecraft, respectively. HRSC has a ground spatial resolution of 10 m/pix at nominal orbit (Jaumann et al., 2007) , and CTX has a ground spatial resolution of approximately 6 m/pix (Malin et al., 2007). Other available images of the ROI include those taken by High Resolution Imaging Science Experiment (HiRISE, McEwen et al., 2010). However, they were not utilized because these images do not capture a continuous area in the ROI and have a scale that is too fine for use over the extended study region.

The ROI is covered by four HRSC Digital Terrain Models (DTMs) with a spatial resolution of 50 m/pixel and meter-scale elevation resolution (See APPENDIX A). Using

DTMs allows for elevation-based analyses, such as estimations of strain. Elevation uncertainty of the DTMs was not provided, however Gwinner et al. (2010) suggest that the uncertainty varies from image to image depending on the observation geometry and surrounding topography. Gwinner et al. (2010) also suggest that when modeling elevation from optically-derived data, the precision of the model is reliant upon the ground spatial resolution of the source images, the angle of incidence, the amount and extent of topography in the image, and the contrast between internal objects. They further estimate that there is a three-dimensional point accuracy of approximately 10 m based on the DTMs in their case study. This validates the use of HRSC DTMs for large-scale surface investigations.

CTX data were downloaded which intersected the HRSC DTMs for a total 61 images (See APPENDIX A). These data were chosen because the CTX provided continuous coverage of the ROI at a scale that allowed resolution of the large-scale linear surface features.

2.3 IMAGE CALIBRATION AND IMPORTATION

USGS ISIS3 was used to calibrate and project the CTX images over the ROI as well as to convert the images into an ArcGIS compatible format. Figure 6 illustrates the calibration and projection process.

HRSC DTMs publicly available through the Planetary Data System (PDS) were projected in a format compatible with ArcGIS. These DTMs are calibrated to the areoid reference and the global Mars Laser Altimeter (MOLA) map. Using areoid-referenced DTMs allows meter-scale elevation information about the ROI to be gathered as 8-bit

signed (positive and negative values above and below the areoid, respectively).

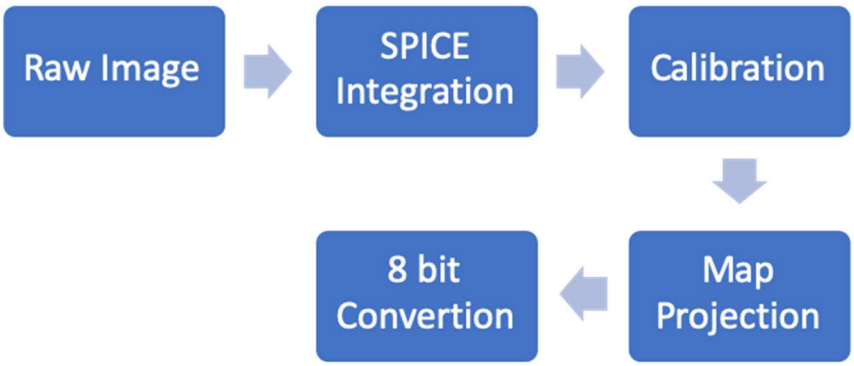

Figure 6: Generic illustration of the image calibration, projection, and conversion (into an ArcGIS readable format) process utilizing USGS ISIS 3. SPICE is information encoded in kernels which summarize Spacecraft Planet Instrument C-matrix Events, or the pointing information of a spacecraft. SPICE allows for raw image data to processed and compared other images and georeferenced.

2.4 GEOMORPHOLOGIC AND STRUCTRUAL ANALYSIS

2.4.1 Geomorphologic analysis

ArcGIS was used to produce a geomorphologic map (11 different unit terrains) of the region as well as a structural feature map of the area (3 types of faults). Terrain units were identified primarily through visual analysis and were based upon surface geomorphology, topography, and albedo. Unit type determinations were also informed through mapping of structural features, and Thermal Emission Imaging Spectrometer (THEMIS) Day IR global maps (Edwards et al., 2014).

2.4.2 Strain Analysis

Structural analysis was used to numerically quantify the extension of the faults within Claritas Fossae. Structural analysis included comparison of large- and small- scale

extension and strain over six graben sets and the northern large Thaumasia graben (Figure 7).

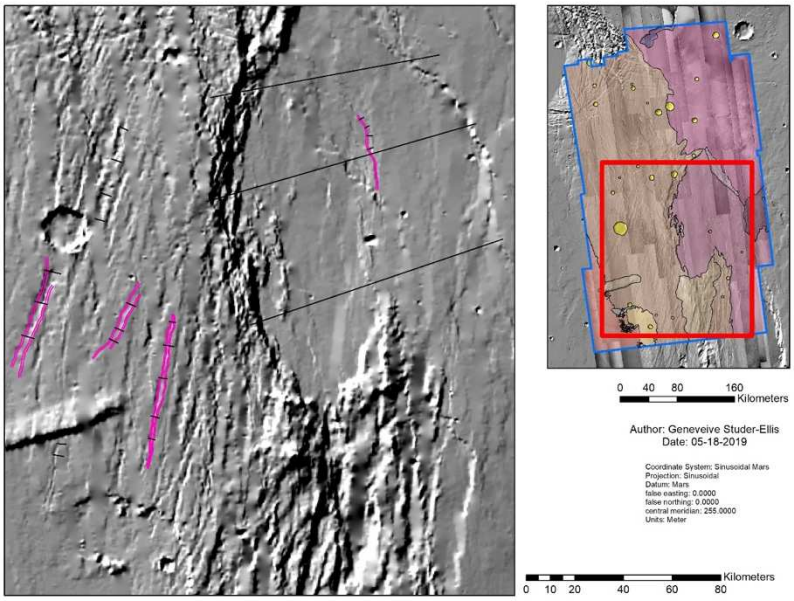

Figure 7: Location image of profiles taken for structural analysis. Black lines are across fault profiles, pink lines are along-strike profiles.

A limited number of graben sets were chosen to be sampled using the following criteria: near-parallel fault sets, lack of crosscutting over sampled fault, and located across the ROI yet within the HRSC DTM. The scope of this study restricted the number of graben sets analyzed to six plus the large Thaumasia graben. Surface extension was determined using the following equations:

$$\Sigma Dei = \frac{\Sigma \mathrm{Dvi}}{\tan \alpha} \quad (1)$$

$$l_i = l_f \ - \Sigma Dei \quad (2)$$

$$\epsilon = \frac{l_f - l_i}{l_i} \tag{3}$$

$$\%\, strain = strain * 100 \tag{4}$$

where l_f is final length, ΣDvi is vertical component of slip (throw), tan(α) is tangent of 60 degrees (assumed for these normal faults), ΣDei is horizontal component of the slip (heave), and l_i is initial length, and ϵ is extension or elongation.

This study assumes Andersonian normal faulting mechanics where σ1 is vertical and σ3 is horizontal. Additionally, we assume that rocks have an internal friction angle of 30°. The combination of those assumptions means that normal faults will dip at 60° and this justifies our use of 60° in this study. Additionally, the Hauber and Kronberg (2005) study uses the same assumption of a 60° dip. Figure 8 graphically describes the extension equations. This strain analysis and computation method follows Hauber and Kronberg

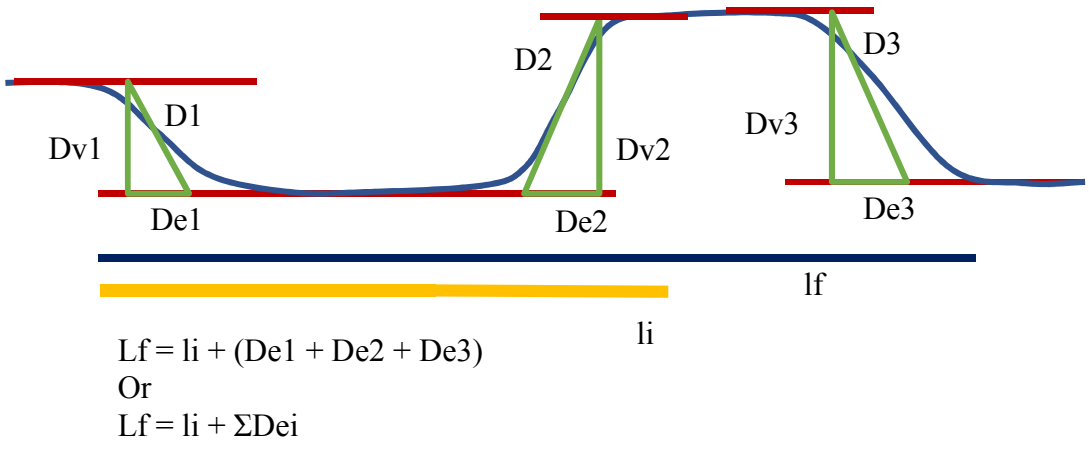

Figure 8: Graphical illustration of the measurements used in the strain equations for this study. Because the equations in my study use summations of vertical and horizontal components, they are flexible enough to be used on individual grabens or any combination of fault and graben sets. Dv are vertical components to slip, De are horizontal components to slip. Note, that even though this illustration depicts slip as containing only a normal component because I calculate cumulative extension based off cumulative height difference, I can account for slip having strike and normal components.

(2005) and is compared to their results. Extension was measured across regional and local profiles. Elevation samples were produced using the ArcGIS interpolate line tool with the 3D Analyst plug-in to create data sets of distance across fault sets versus elevation (all in m) with the elevation data pulled from the HRSC DTMs.

2.4.3 Along strike throw-profile analysis

Additional structural analysis included along-strike analysis of elevation differences between the top and bottom of faults in the manner of Manighetti et al., (2001). Each along strike analysis was completed along one side of a graben. Elevation profiles are along either side of the fault trace. The hanging wall elevations were subtracted from the footwall elevations. This results in a differential profile that provides information about the fault's propagation behavior. Seven different faults were analyzed with profile traces across the top and bottom of the fault at various widths (described in Chapter 3) using the Stack Profile tool in ArcGIS to export a spreadsheet with elevation across line. Excel was then utilized to find the differences between the top and bottom of the fault to identify along strike extension patterns and display them graphically.

2.4.4 Sector Diagram Analysis

Sector/Rose diagrams of each fault type were produced to illustrate dominant orientation trends. Generic Mapping Tools (GMT) and the subprogram PSRose were used to produce the diagrams sample script in Figure 9. Three script runs were completed, one for each fault type identified in the structural mapping.

```
psrose WholeMapNormalFaultCertainPSTable.txt -i0 -A5 -R0/900/0/360 -S5c -Bxg100 –Byg30 -
B+t"Certain Normal Faults Sector Diagram" -Gred -W0.5p > WMNFC_Run2.ps
```

Figure 9: Example script for implementing the PS Rose function in GMT. This script imports a table that is a list of azimuths, bins the azimuth counts into 5-degree categories; then crates a sector diagram with lines every 30-degrees, for a full 360-degree diagram, and "count" marks every 100 counts. The script adds a count legend, and a title then exports the diagram as a specific named file.

2.4.5 Surface Age Analysis Through Crater Counting

Crater age estimates for the Dissected Highlands (DH) as well as the two main graben swarm centers (Upper Left (UL), and Lower Right (LR), were produced. Figure 10 shows the crater counts and area counted in for the age estimates of the DH. This

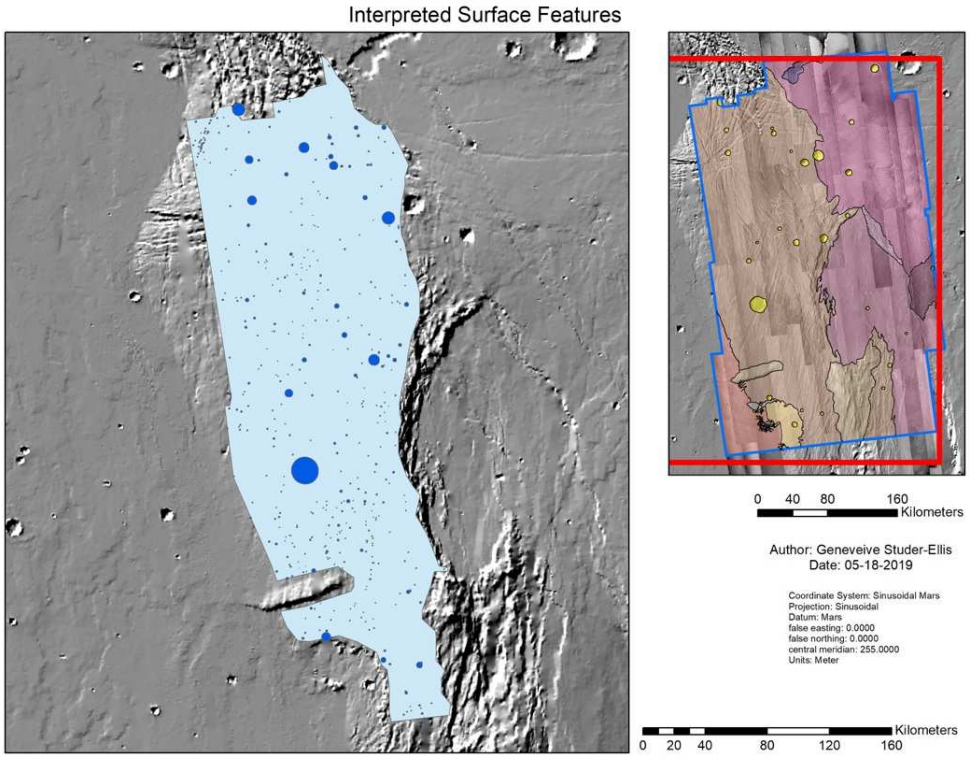

Figure 10: Area and craters identified in the DH for absolute age analysis. Dark blue are craters counted in the DH analysis, while light blue is the area utilized for the CSFD of the DH.

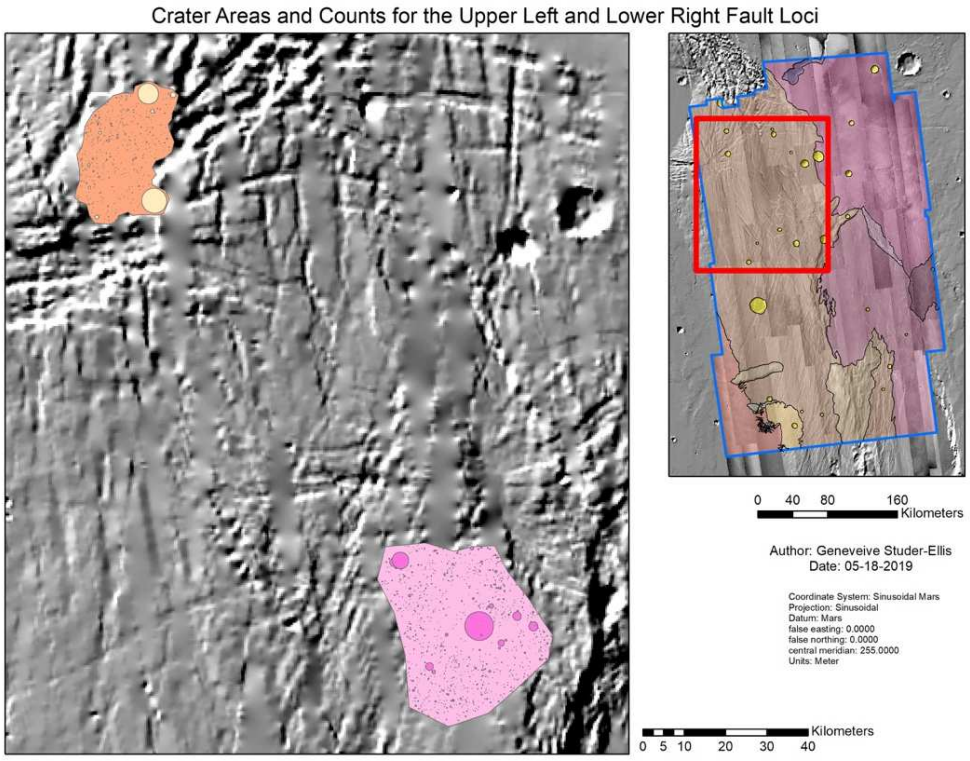

Figure 11: Areas and craters identified in absolute age analysis of the upper left (UL) and lower right (LR) swarm sections. These crater counts were completed to determine the background age of the DH. The UL contains craters (light orange) and area used for computational analysis (dark orange). While the LR contains craters (dark pink) and area (light pink).

crater analysis was completed to determine an absolute model age of the surface in the DH including resurfacing events. Figure 11 shows the crater counts and areas counted in the UL and LR locations; these counts were conducted to determine an absolute model age for the original emplace surface of the DH before extensional events occurred. The UL and LR counts utilize crater counting across CTX images which provide fine enough spatial resolution to identify craters small enough for their count to have not been affected by the resurfacing (extensional) events. The scope of this project limited the counting area for the UL and the LR samples. Data collected for the UL location was insufficient in area to provide a CSFD, which could be fit with a model age. Crater counts

were accomplished with the aid of CraterTools (Kneissl et al., 2015, 2011) and Craterstats (Michael, 2013; Michael et al., 2012; Michael and Neukum, 2010; Neukum, 1983; Platz et al., 2013) with spatial analysis in ArcGIS. Crater count areas were identified for the three datasets and then complete crater counting was performed down to the spatial limit of the sampled image(s) (CTX images at ~10s of m for the swarm centers, and THEMIS Day IR at ~500 m for the Dissected Highlands) using the CraterTools plug-in for ArcGIS. The sampled areas for UL was $6.02x10^2$ km^2, LR was $1.28x10^3$ km^2, and DH was $4.12x10^4$ km^2.

Craters were identified as circular, or near circular ground depressions that contained a rim and were not arranged linearly. Randomness analysis was conducted via Craterstats to determine if the population of craters was polluted with secondary impacts (if a size of crater was too ordered via the analysis it was determined to be contaminated with secondaries and was not used to fit ages). Each dataset of crater diameters was exported with the accompanying area shapefile for cartography in ArcMap. Craterstats was utilized with the crater production function of Mars, Ivanov (2001) and the crater age function of Mars, Hartman and Neukum (2001) to determine absolute ages and epochs (Michael, 2013). The preceding functions were used because they were previously used in the area by Tanaka et al. (2014), which allowed for direct comparison between datasets. Age fits were completed using Poisson fits (Michael and Neukum, 2010).

CHAPTER 3

RESULTS AND DISCUSSION

3.1 GEOMORPHOLOGIC MAP AND UNIT CLASSIFICATION

Across the Region of Interest (ROI) in Claritas Fossae, I identified 11 geomorphological units (Figure 12), which can be classified into three categories; highlands, midlands, and lowlands. Figure 12 shows the ROI and the locations of unit example areas highlighted with yellow boxes. A summary of these units, their main features, and their interpreted origin can be found in Table 2.

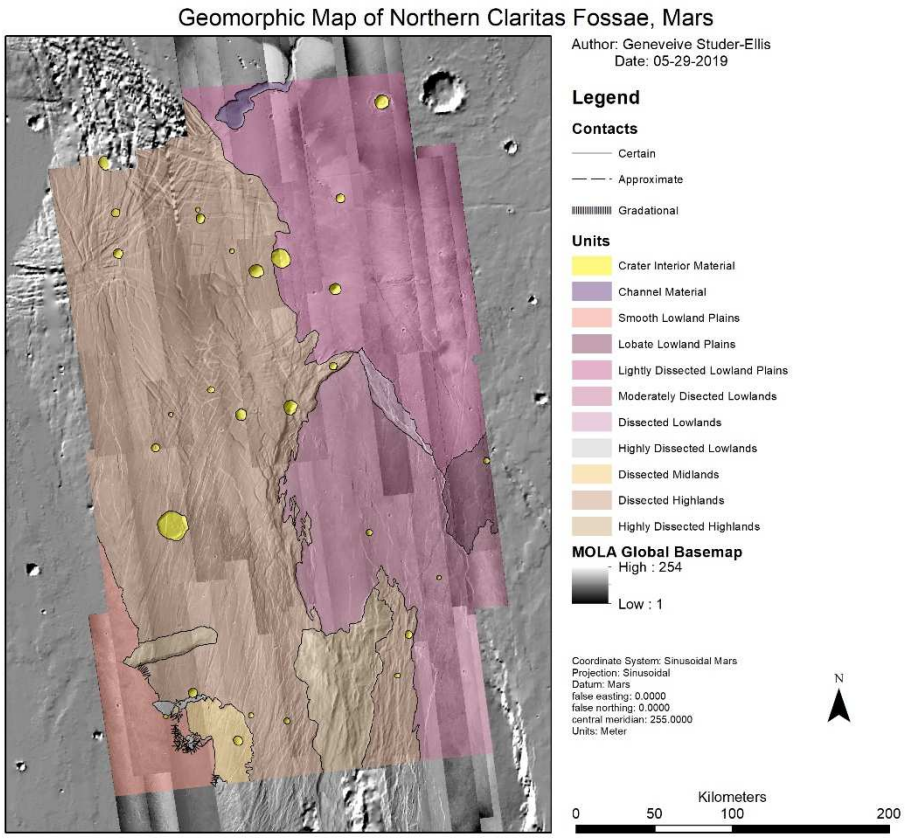

Figure 12: Geomorphologic map of the ROI created in this study.

Table 2: Summary of geomorphic units identified in this study, ordered from youngest to oldest. Continues next page. See mapping in figures 14-17.

Unit Name	Label	Unit Description	Interpretation
Crater Interior Material	CriM	Contains the ridge and inside rim of craters, characterized by circular bowl-shaped depressions in the landscape that may be surrounded by an ejecta blanket, typically have a raised rim and sometimes a central uplift	Craters formed by impacts, including rim material but not ejecta
Channel Material	ChM	Sinuous depression ending in oblate depression, typically with scalloped edges where lobe-like depressions are infilled by dust and debris	Rille produced through possible volcanic erosion and or collapse
Smooth Lowland Plains Material	SLP	Characterized by dimpled topography in low relief, presents as smooth and non-lineated	Young volcanic unit
Lobate Lowland Plains Material	LLP	Knobby lobate topography with dimpled surface and sparse linear features of moderate relief	Different young volcanic unit
Lightly Dissected Lowlands	LDL	Knobby dimpled unit in low relief with moderate linear features of higher relief dissecting the surface.	Young volcanic unit with minimal pull apart scars
Moderately Dissected Lowlands	MDL	Flat unit dissected by moderate relief (~50-1000 m) linear features	Slightly older volcanic unit with moderate pull apart scars
Dissected Lowlands	DL	Knobby surface dissected by numerous moderate relief (~50-100 m) linear features	Possibly down-dropped dissected highland block
Highly Dissected Lowland Material	HDL	Characterized by dimpled and knobby topography across flat extent	Heavily eroded volcanic unit
Dissected Midlands	DM	Similar topography to the DH unit, this unit also displays a lineated horst and graben topography but at a lower elevation and lower relief	Possibly down-dropped dissected highland block
Dissected Highlands	DH	Characterized by lineated horst and graben topography as well as large relief (~100-200m) outcrops of knobby terrain	Highland plains units, heavily stretched apart, possibly Noachian or early Hesperian based upon age estimates derived from crater counting analysis as well as Tanaka et al., (2014)

Heavily Dissected Highlands	HDH	Characterized by rolling and dimpled topography with decayed linear feature remnants of Dissected Highlands materials	Highland Plaines unit, heavily stretched apart and eroded, possibly late Noachian or Early Hesperian based upon Tanaka et al. (2014)

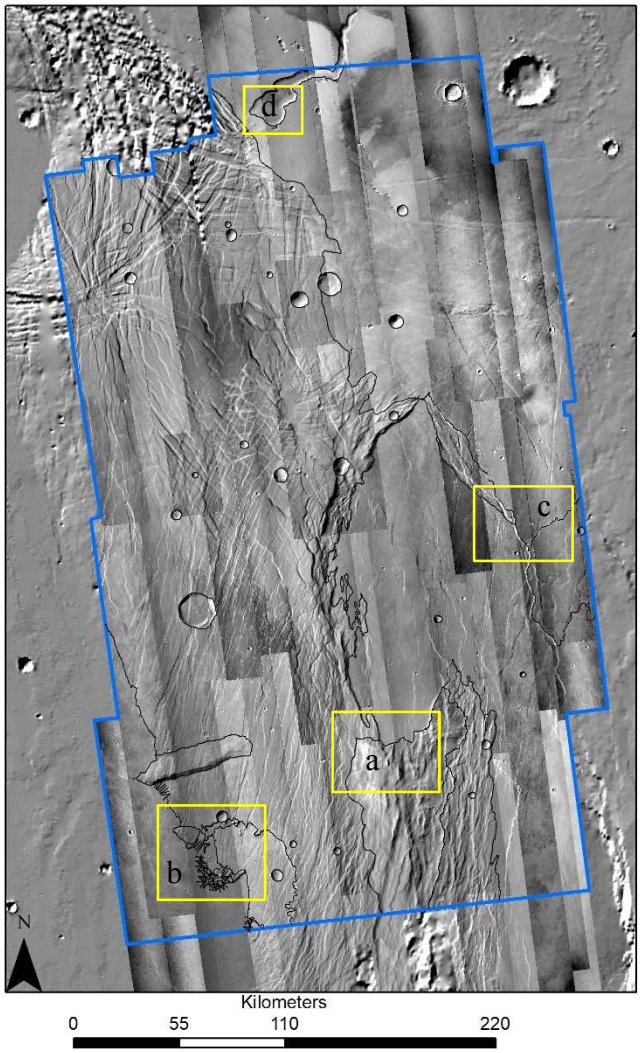

Figure 13: Region of Interest (ROI) with yellow boxes highlighting the location of figures 14-17 (as a, b, c, and d respectively) which contain typical unit extents for each of the units classified in this study.

The highlands contain two units, the Heavily Dissected Highlands (HDH), and the Dissected Highlands (DH). Typical unit examples for the HDH and the DH are shown in Figure 14. The HDH are estimated to be the oldest, most heavily eroded and weathered unit. The DH are estimated to be slightly younger, than the HDH, and contains two loci or focuses of graben swarms (described in subsection 3.2). The DH appears stretched in an E/W direction with a higher elevation on its eastern edge. Age estimations for DH are discussed in subsection 3.6.

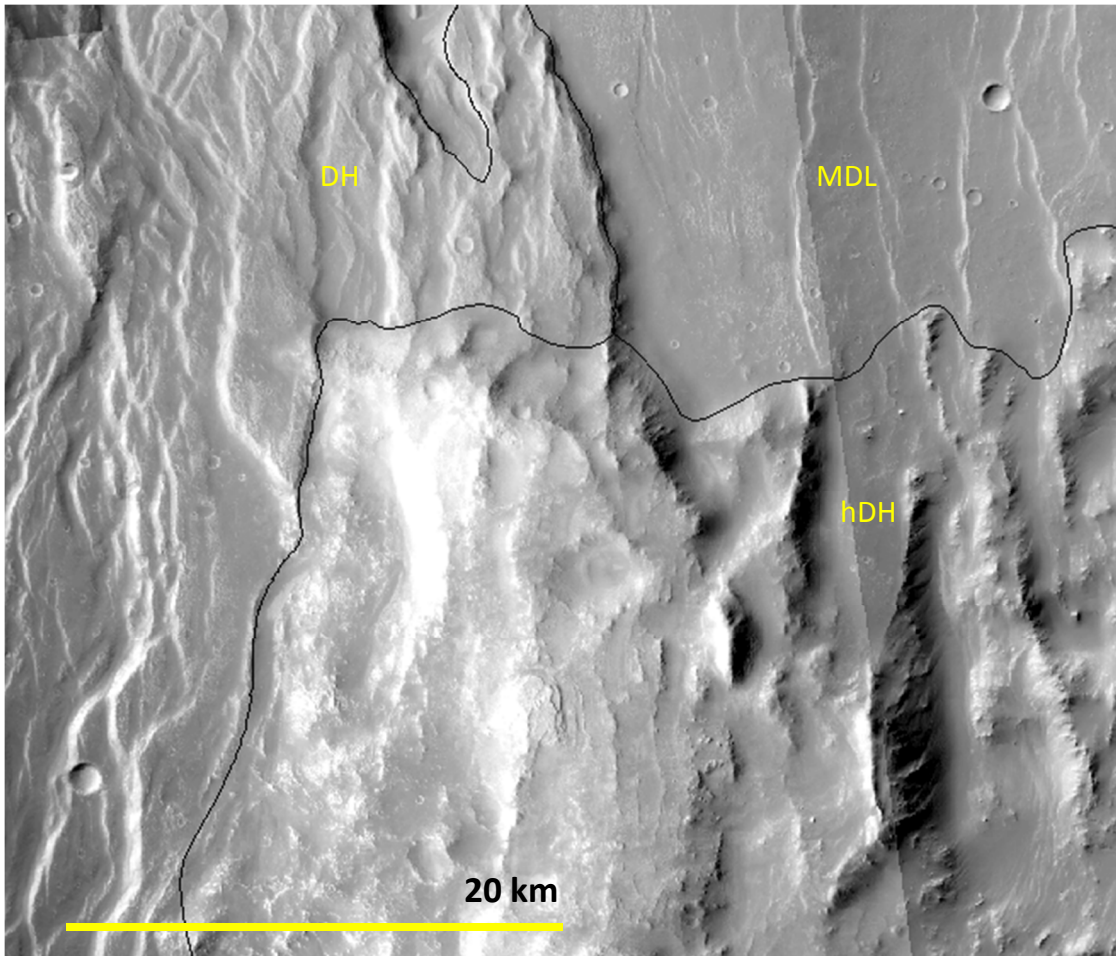

Figure 14: Typical unit examples for the Dissected Highlands (DH), the High Dissected Highlands (HDH) and the Moderately Dissected Lowlands (MDL). Units are identified by acronym in yellow and contacts are solid black lines between the units.

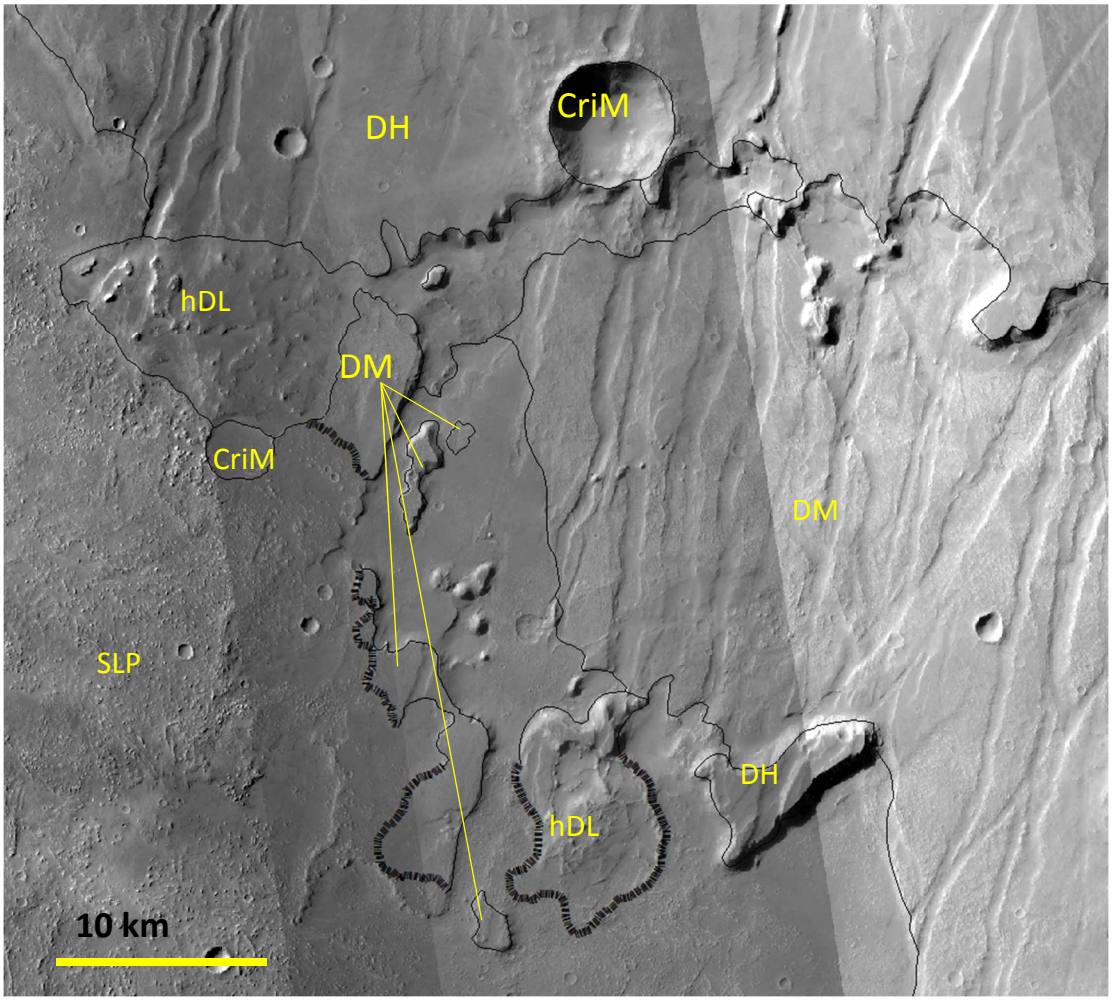

Figure 15: Typical unit examples from the highlands, midlands, and lowlands; including the Dissected Highlands (DH), Dissected Midlands (DM), Highly Dissected Lowlands (HDL), Smooth Lowland Plains (SLP), and Crater Material (CriM). Units are identified by acronym in the image in yellow, and contacts between units are in black (solid line for certain contacts, and dashed line for gradational contacts).

The midlands contain one unit, the Dissected Midlands (DM). The DM appear geomorphologically similar to the DH with only average elevation differentiating the units. It is possible that the DM is down-dropped DH. A typical unit example for the DM appears in figure 15.

The lowlands contain eight units: Highly Dissected Lowlands (HDL), Dissected Lowlands (DL), Moderately Dissected Lowlands (MDL), Lightly Dissected Lowlands (LDL), Lobate Lowland Plains (LLP), Smooth Lowland Plains (SLP), Channel Material (ChM), and Crater Material (CriM). Figures 13-16 show typical unit examples for the lowland units. The lowlands have undergone a multitude of processes over time (detailed in Figure 35), but in general have similar interpreted origins, some form of volcanic emplacement followed by minor extension. The HDL provenance has undergone

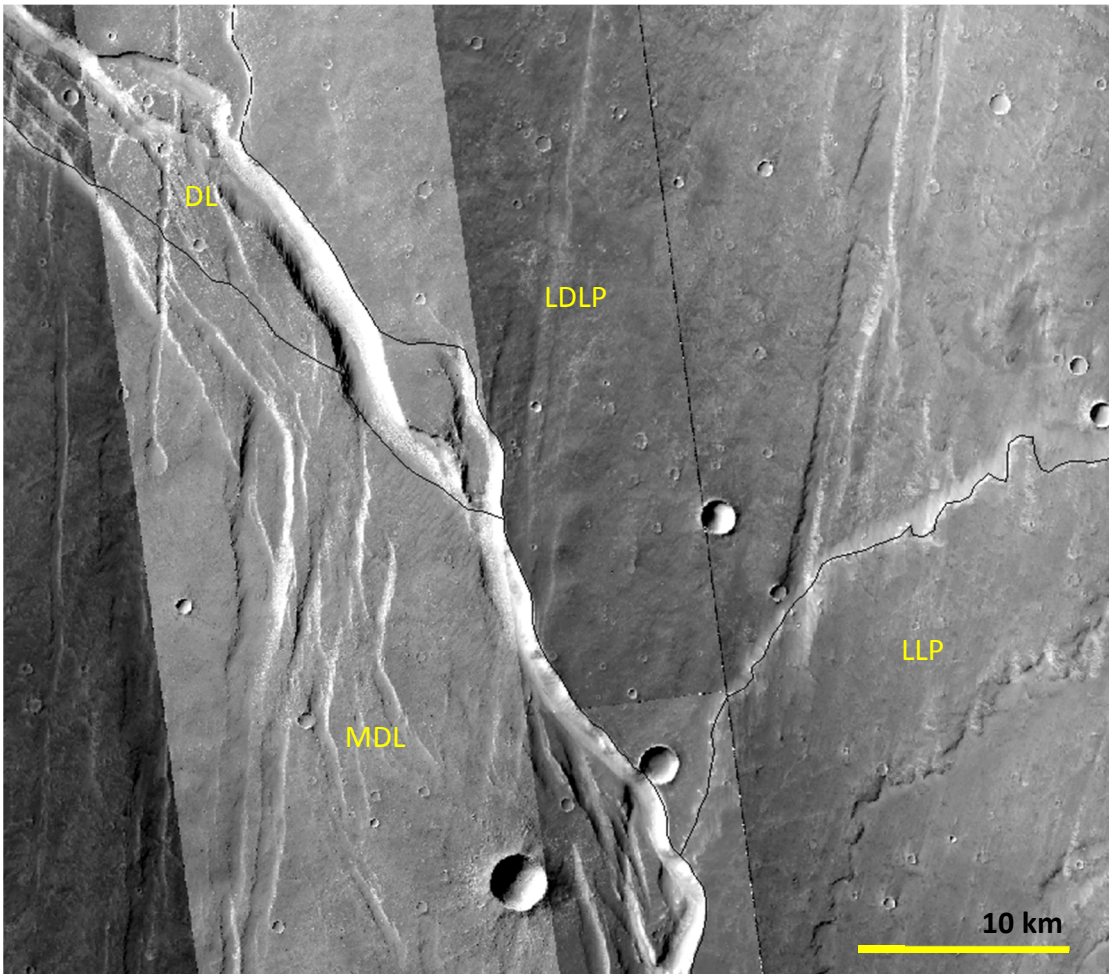

Figure 16: Typical unit examples for several lowland units including the Moderately Dissected Lowlands (MDL), Lobate Lowland Planes (LLP), Dissected Lowlands (DL), and Lightly Dissected Lowland Planes (LDLP). Units are identified in yellow by their acronyms and contacts between units are black lines (solid line for certain contacts, dashed line for approximate.

significant weathering and erosion leaving behind a surface with dimpled and knobby terrain and no linear features. The DL and the MDLs appear very similar to each other with differences in the degree of dissection by extension and structural lineation. Both the DL and MDL are interpreted to be volcanic flows overwritten by extensional structures. However, the MDL is younger, occurring in the Hesperian as opposed to the DL Noachian age, with extensional structures which propagate at slightly different azimuths (more N-S than NNE-SSW). The LDL are a volcanic flow with minimal linear features interpreted to be extensional faulting. The LLP unit is a volcanic unit overprinting the LDL and containing few linear features.

The SLPs are interpreted to be volcanic flows abutting the highlands and overprinting the western edge of the DH. ChM is interpreted to be a collapse feature from a volcanic tube and ponding area. CriM are interpreted to be impact formed craters.

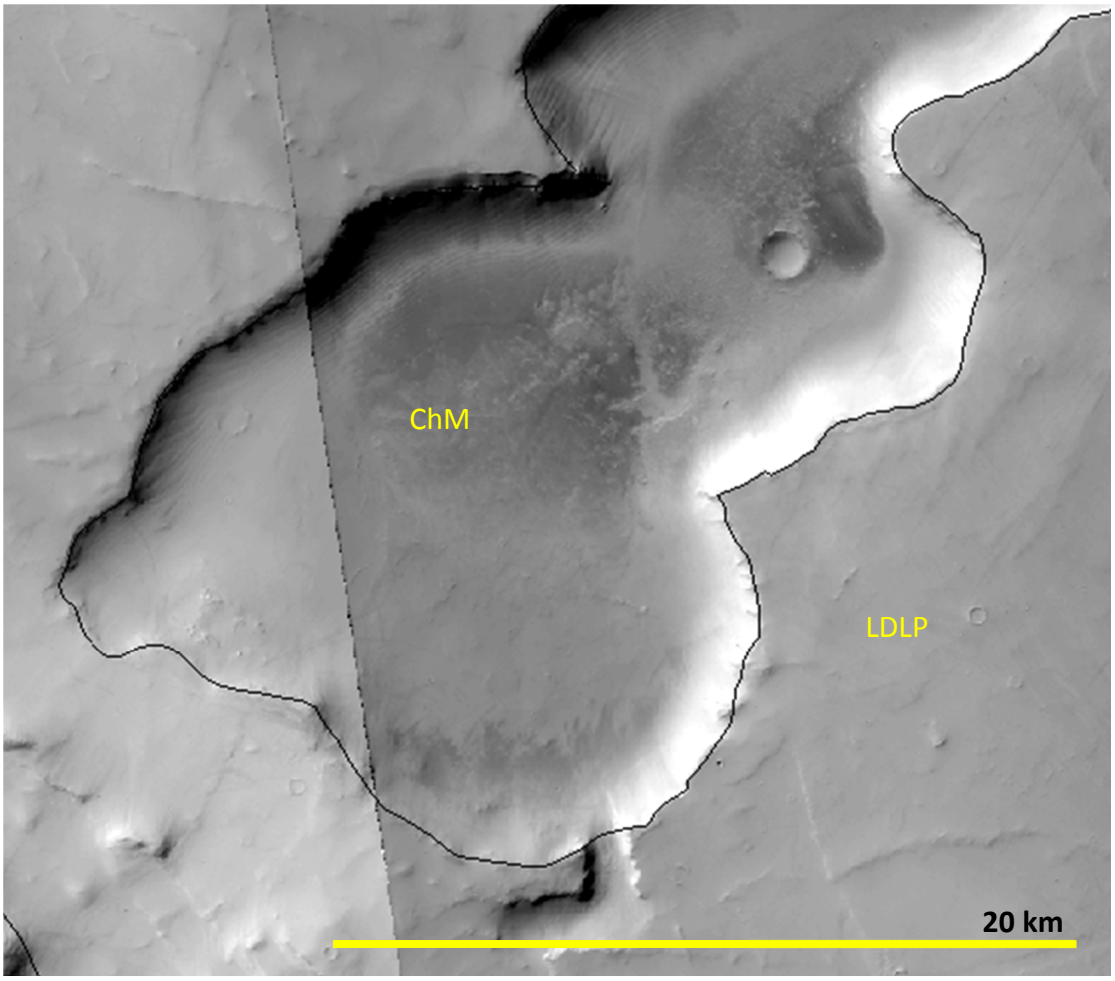

Figure 17: Typical unit examples for Channel Material (ChM), and Lightly Dissected Lowland Plains (LDLP). Units identified by their acronyms in yellow and contact between units is a black line.

3.2 STRUCTURAL MAPPING

Figure 17 shows a structural feature map of all 9,052 identified fault traces. They are interpreted as falling into three categories; normal faults (8,810), uncertain normal faults (103), and uncertain faults (139). Linear features were identified through visual analysis and interpretation of the CTX, on the Mars Reconnaissance Orbiter, MRO) images. The features were classified based on visual parameters, as detailed below.

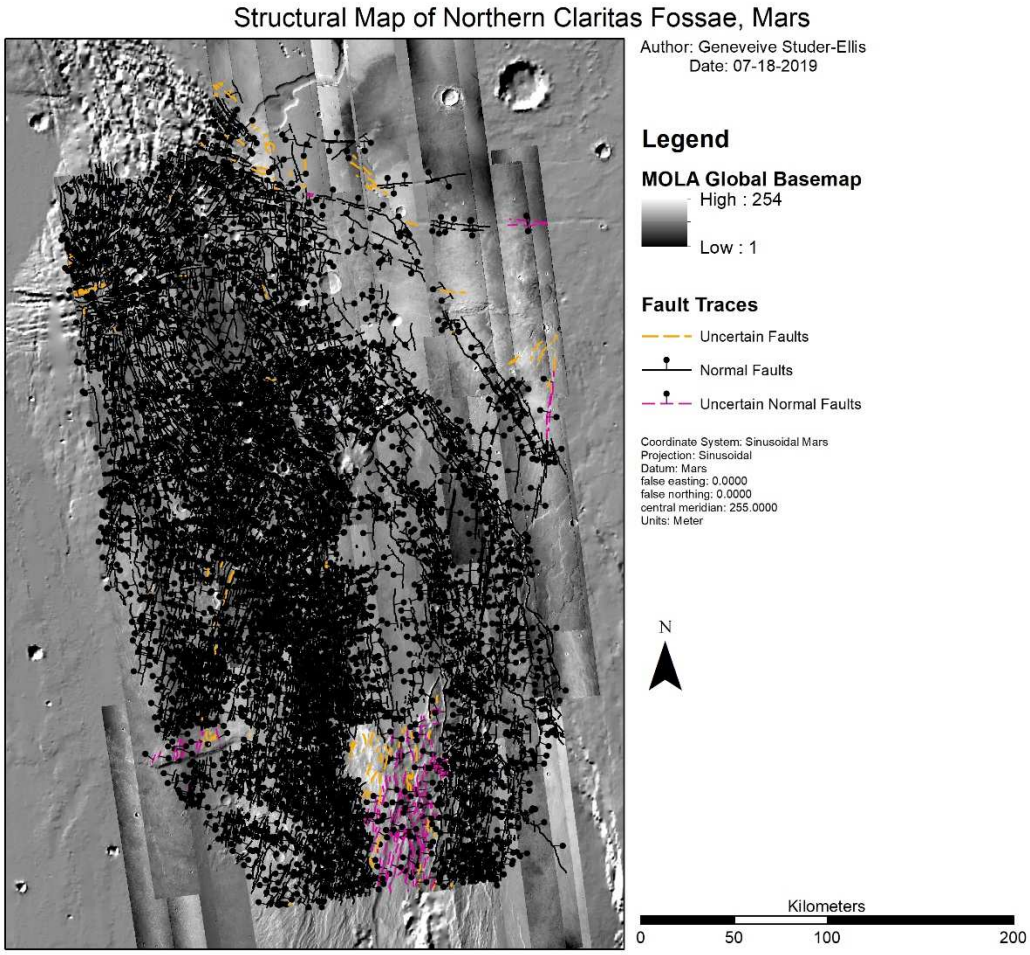

Figure 18: Structural map of the ROI, produced using ArcGIS by ESRI.

Normal faults were identified as consistent linear features with distinct separate down-dropped and uplifted surface blocks usually occurring in pairs to produce horst and graben topography. Normal faults were identified and interpreted as such because they frequently occur in parallel or near parallel sets, within an extensional regime, and display down-in graben pairs. However, the dip of faults cannot be identified because of resolution limitations from CTX.

"Uncertain normal faults" were identified as linear features which are discontinuous and appear to start and stop, non-distinct uplifted block surfaces, probable down-dropped block, and weathered/eroded edges to scarps. Non-distinct uplifted block surfaces are surfaces that appear to be uplifted relative to the surface on the opposite side of the fault, but do not display a "flat top." The same irregular surface describes the probable down-dropped block description. "Uncertain faults" are linear features whose identity cannot be confirmed. They are discontinuous across the surface, unidentifiable down-dropped/uplifted block sides, or ridge-like appearance indicating possibly eroded horst to point history. discontinuous lengths or extents are linear features that appear to stop and start when viewing the surface in planar view.

The structural feature map reveals two distinct "swarms" of faulting inside the DH, as well as other non-swarming faulting across the younger surfaces. The DH swarms are located in an upper left (UL) and lower right (LR) pattern inside the unit (Figure 19). The LR pattern of faulting (propagating in a NE/SW manner) appears to have occurred first, because of cross-cutting from faults originating in the UL (propagating in a NW/SE manner) (Figure 20). There are instances where faults originating from the LR cross-cut faults from the UL, but these occurrences are less frequent. Therefore, I conclude it is likely, that the LR faulting occurred first followed by the UL some time later. Resurfacing age estimates are discussed in Subsection 3.6. Other faulting across the region occurs on surfaces estimated to be younger than DH (by reregistering the location with the Tanaka et al., 2014 global Mars map) and appear in non-swarming or clustered swaths, characterized by visual examination, with the exception of a possible smaller swarm MDL.

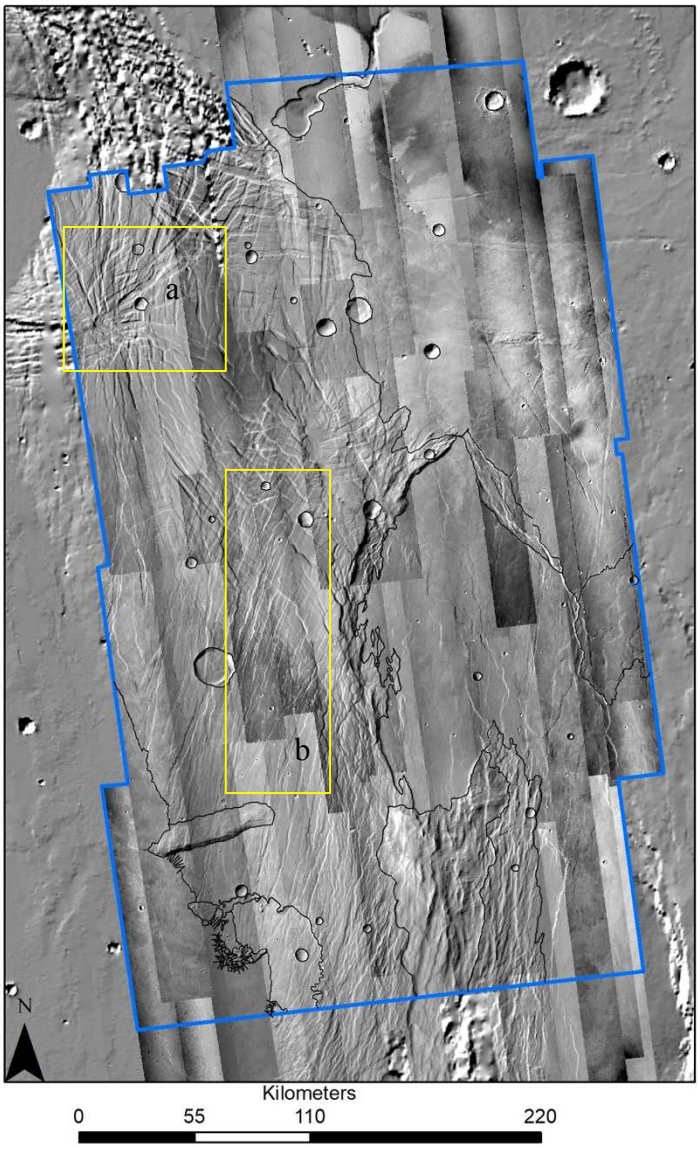

Figure 19: Approximate locations of the two graben swarms in Claritas Fossae. (a) is the UL swarm, and (b) the LR swarm. The UL swarm has a radiating pattern while the LR swarm has a sub-parallel pattern.

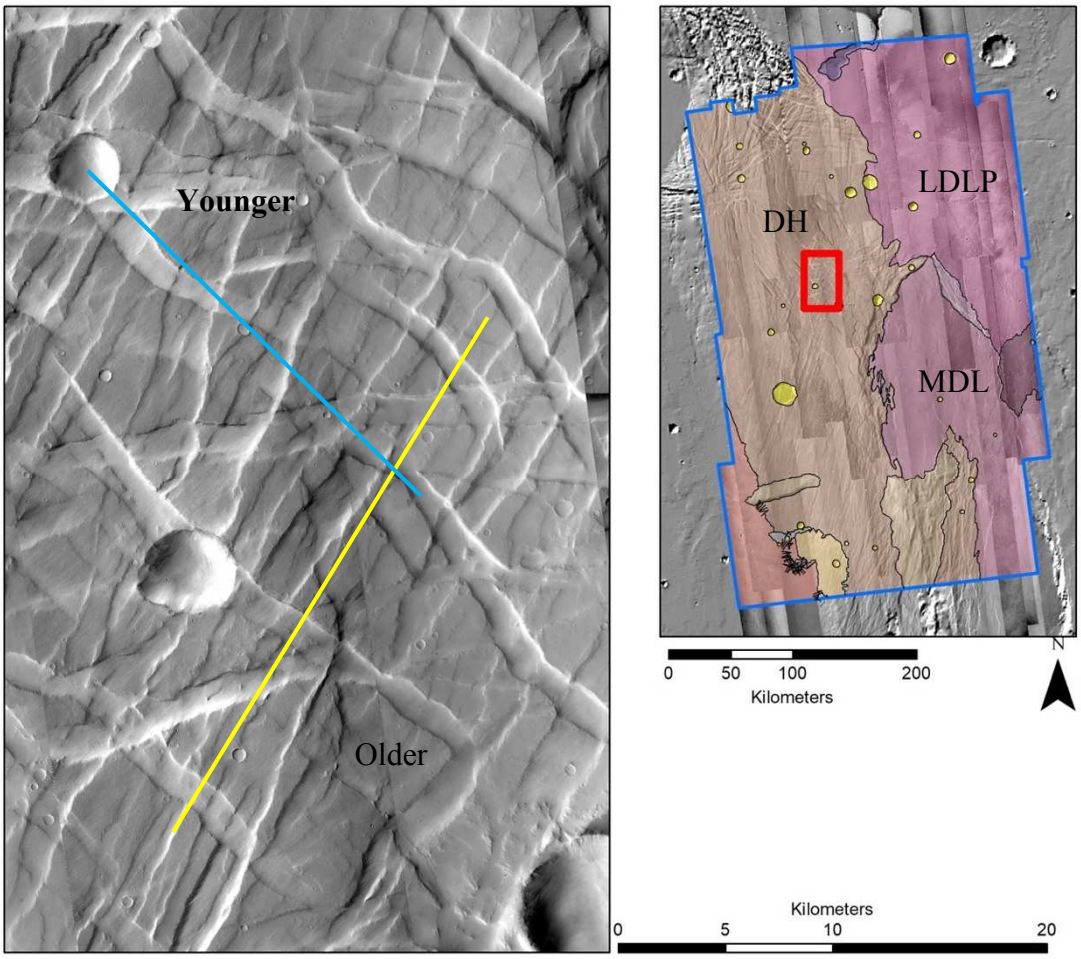

Figure 20: Portion of the DH (left) showing the cross-cutting relationship between the LR and the UL graben swarms and a location map (right) showing where the left figure is in relation to the whole ROI. Left image shows two distinct sets of faults propagating in NE/SW and NW/SE; these faults originate in the LR and UL loci, respectively. The image shows how the faults originating in the UL cross-cut and deform the faults originating in the LR, indicating that they are younger. In yellow is an example fault trace from the LR, in blue is an example fault trace from the UL. The example fault traces follow the cross-cutting pattern described here.

3.3 ACROSS STRIKE STRAIN

In Chapter 2, six smaller graben systems were identified in addition to the northern extent of the large Thaumasia graben (identified in Hauber and Kronberg, 2005). Figure 6 in (Chapter 2) shows the placement of the grabens across the ROI. Quantifying extension allows me to determine if extension was consistent across the region or if local pockets experienced differing deformation regimes. Strain percentages allow for the comparison of a regional and local extension not just region-to-region or location to location. If the strain is similar within a few percentage points, this indicates consistent strain across the system. An average strain percentage was calculated across each of the smaller graben systems individually, as a class, across the Thaumasia graben, and across all measured sets. Standard deviation calculations were used to analyze the variance in strain percentage calculations. Averages and standard deviations are detailed in Table 3. Extension and strain calculations for each graben set are listed in APPENDIX B.

Table 3: Average of strain percentages and standard deviation of those averages, across each graben set individually, the large Thaumasia graben average, all six large-scale grabens, and all of the grabens across the study area.

Graben Set	Average Strain Percent	Standard Deviation	Number of Samples
1	4.47	1.94	4.00
2	4.35	1.07	5.00
3	4.54	0.21	3.00
4	2.60	0.92	3.00
5	7.78	4.08	4.00
6	3.58	1.40	4.00
Thaumasia Graben	1.12	0.32	3.00
Large Scale (Average)	4.22	2.56	23.00
Total (Average)	4.22	2.56	26.00

I analyzed two profiles across two grabens in graben set 1 (Figure 21). This figure shows the profiles and the measurements (ΣDvi and l_f as detailed in Figure 7, Chapter 2) derived for them, as well as simplistic 2D graphical representations of the calculations used (Chapter 2) to derive extension through calculations. I analyzed five profiles across a graben in Graben set 2. I analyzed three profiles across a graben in graben set 3. I analyzed three profiles across a graben in graben set 4, I analyzed four profiles across a graben in graben set 5, I analyzed four profiles across a graben in graben set 6, and I analyzed three profiles across the TG in graben set TG.

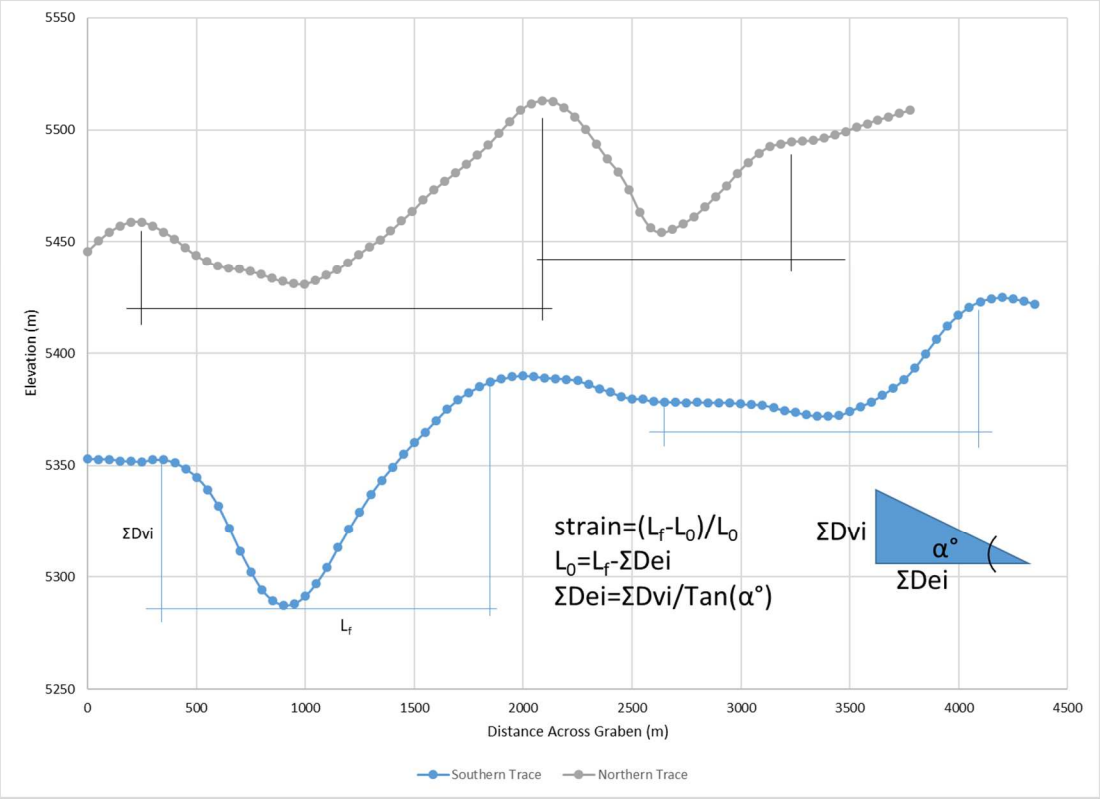

Figure 21: Graphical representation of the profiles taken across graben set 1. The northern profile is in grey, and the southern profile is in blue. This image also displays a simplified strain calculation triangle which shows the relationship between the angle of extension (α) which is assumed to be 60°, maximum vertical offset (ΣDvi), how I calculate maximum horizontal offset (ΣDei), initial length (l_i), final length (l_f), and strain.

Appendix C contains graphs for each graben set showing the profiles and locations of measurements. Each graben set has similar strain values. Strain percentage values found in this study are similar to values calculated by Hauber and Kronberg (2005) of 0.5 – 3.0% (Table 4) and minor variance is expected to be caused by sampling site differences. Hauber and Kronberg utilize the same strain equations as my study (their notation is slightly different using e_{cum} instead of ΣDei, D_{cum} instead of ΣDvi, L_{final} instead of l_f, and l_0 instead of l_i) across the majority of the large Thaumasia graben. They use topographic data derived from the Mars Orbiter Laser Altimeter (MOLA), specifically gridded DTM. They use a dip angle of 60° the same as my study. Figure 22 shows the locations of the profiles taken in Hauber and Kronberg. Samples two and three from Hauber and Kronberg are taken in locations similar to my samples of the large Thaumasia graben.

Table 4: Estimated change in length (km), and strain (%) values from Hauber and Kronberg (2005).

Sample Number	Change in Length (km)	Strain (%)
1	0.5	2.9
2	1.5	1
3	1.25	1.25
4	3.5	2.5
5	4.1	2.75
6	3.25	2
7	2.1	1.75
8	4.25	2.1
9	3.9	2
10	2.75	3
11	2.5	2
12	3.75	2.9

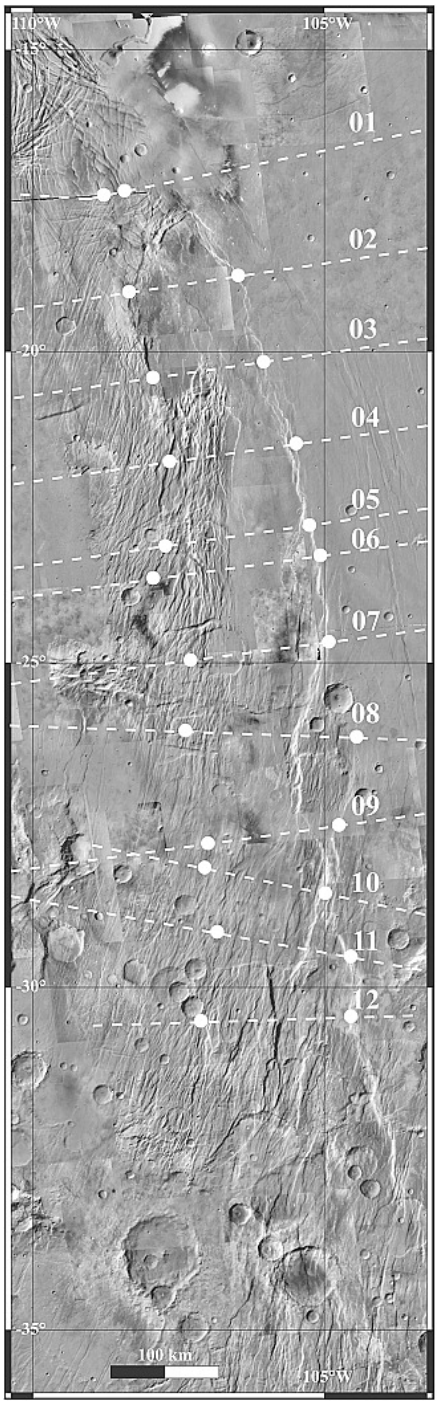

Figure 22: Locations of profiles (white dashed line) across the large Thaumasia graben taken in Hauber and Kronberg 2005. Background is a mosaic of Mars Orbiter Camera – Wide Angle Camera (MOC-WAC) images. White dots denote the l_f used in strain calculations.

3.4 ALONG STRIKE THROW-PROFILES

First-order shape analysis for the along-strike fault throw profiles was conducted on seven fault samples: the left side of graben set 6 and on both sides of graben sets 2, 3, and 4 Figure X. Manighetti et al., (2001) completed along strike fault throw profile analysis in the Afar region of Africa on Earth. They study 255 faults ranging in size from 0.3 to 60 km long. While those lengths are smaller than the faults observed in this study it is common that Mars features scale up compared to their Earth counterparts. Manighetti et al., derived elevation profiles along fault strikes on either side of the fault trace using three high-resolution DTMs. They calculate the maximum throw along the length of the measured fault in the same manner as described in Chapter 2. Manighetti et al., 2001 then plot displacement profiles of normalized throw against normalized length, where normalized is sample n divided by maximum value for throw and length. The faults studied by Manighetti et al., 2001 fall into two slip-length profile categories "unrestricted" and "restricted" profiles. Fault growth patterns, described below, determine the throw-profile pattern.

Faults are assumed to grow linearly from a center point of maximum displacement and propagate outward until they reach a restriction or barrier. If and when a fault encounters a barrier the throw-profile will evolve into an elliptical slip-length profile. Depending on when and where a fault encountered a restriction the slip-length profile will follow a pattern detailed in Figure 23 and described below. Barriers to fault growth include anything that restricts propagation and include increased rock strength, running into another fault, running into a ductile material that doesn't deform in a brittle manner, or an uneven/dynamic stress field preferentially "pulling" on one side of the

fault. The continuous placement of restriction barriers to a consistent side of faults across a region can be indicative of a deformation field, with asymmetric stress across the field. Deformation fields can impact the fault slip profile on a regional average, thus uniform opening of a rift, or a propagating rift will have differing regional slip patterns (Figure 24).

Using the methods of discussed in Chapter 2, this analysis and results of this study are compared to the first-order shape definitions of Manighetti et al., (2001) shown in Figure 23. Profiles can be classed as restricted or unrestricted.

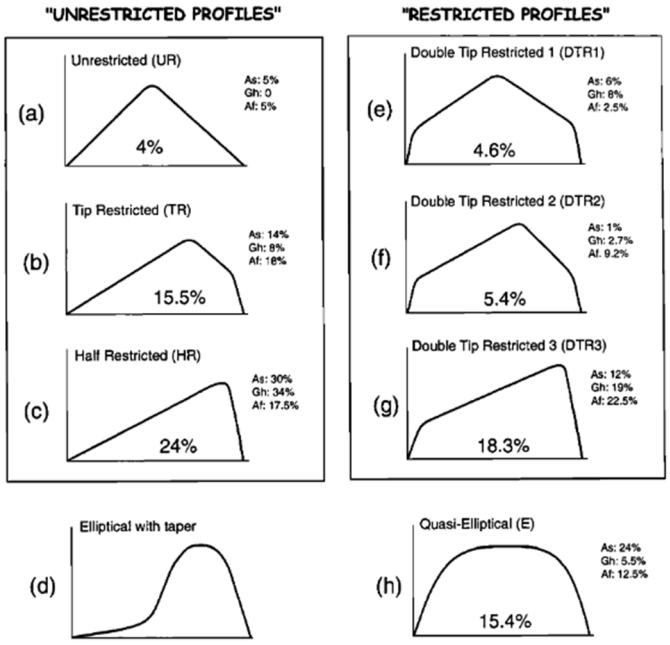

Figure 23: Sketch of first-order shapes adapted from Manighetti et al. (2001). Unrestricted profiles show faults which have either not encountered a barrier to propagation (a), or encountered a barrier on one side only (b and c). Restricted profiles show faults which encountered a barrier to propagation on both sides (e, f, g). Quasi-Elliptical (h) shape profiles occur when a fault continues to grow in displacement but not propagation after encountering barriers to propagation. Tapers (d), or renewed propagation, can occur on any shape profile except (a) but are illustrated only with a quasi-elliptical profile to save space.

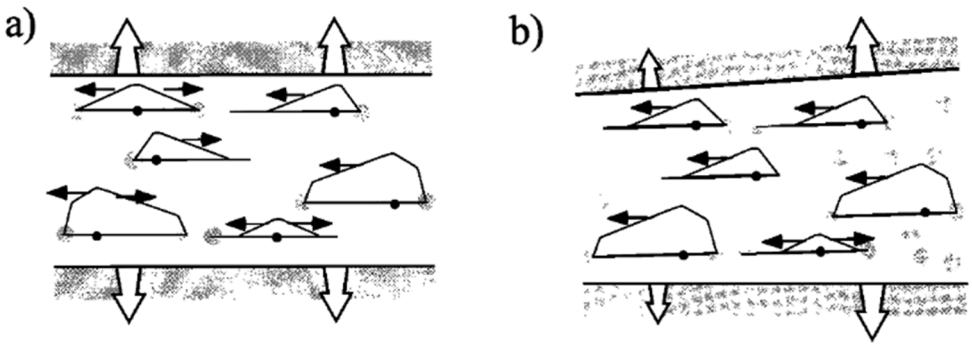

Figure 24: Illustration of (a) uniform and (b) non-uniform distribution field's control over the asymmetry of faults over a region. Adapted from Manighetti et al. (2001).

Unrestricted profiles indicate a fault either did not encounter a barrier while growing, or only encountered a barrier to growth on one side of the propagation. Unrestricted sub-categories include unrestricted, tip-restricted, and half-restricted.

Restricted profiles encounter barriers to fault propagation on both sides of the center point of maximum displacement. Restricted profiles include double tip restricted 1, double tip restricted 2, and double tip restricted 3. Manighetti et al., (2001) also define elliptical-with-taper and elliptical-as-shape options for throw-profiles. These categories allow me to make inferences into fault growth patterns through time, and across a region.

A varied or corrugated appearance along strike is observed both in this study and in Manighetti et al., (2001) and is ignored for first-order shape analysis in both. Each throw-profile figure has first-order shape lines in black to help differentiate between corrugations and shape categories. All graben profiles are plotted with T/Tmax as the normalized values for the difference in height (maximum throw) and L/Lmax is the normalized fault length. This means that values normally range from 0 to 1 in the throw-profile graphs with 0 indicating a small value divided by the maximum value and 1 a

large value divided by the maximum value. This allows faults of differing lengths to be compared to each other.

The left side of graben set 2 displays an unrestricted profile, meaning that there is a maximum elevation differential (throw) in the middle of the fault and the sides linearly decrease with distance from center. This indicates that growth has not reached a barrier to growth on either side of the fault, initial fault growth and maximum displacement is located in the middle of the fault (Figure 25).

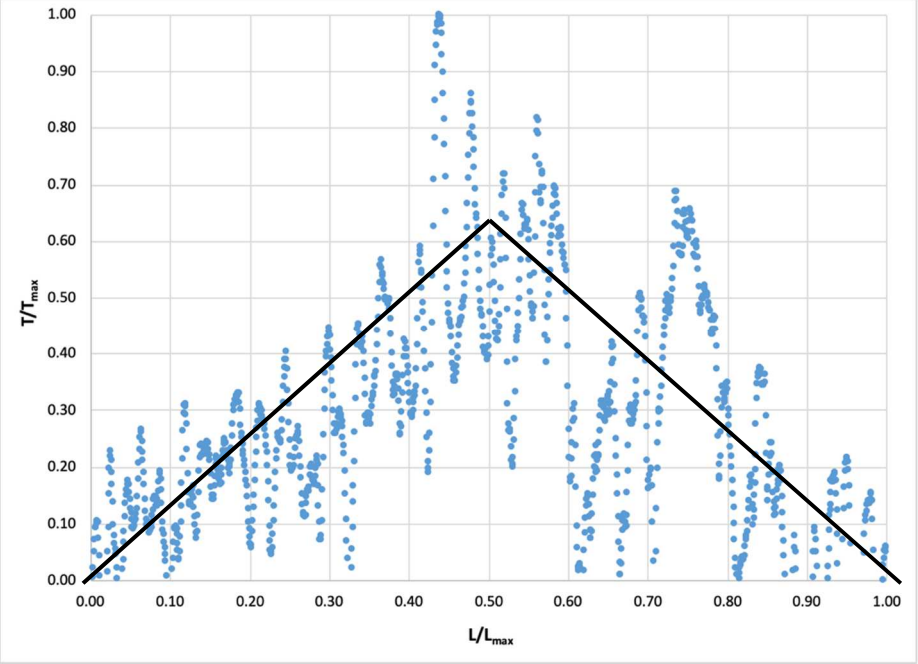

Figure 25: Normalized throw-profile for the left side of graben set 2. Distance between elevation sampled top and bottom of the fault is 500 m. Black lines are interpreted first-order shape and fit an unrestricted profile.

The right side of graben set 2 displays a dip in the first-order shape around the middle of the fault (Figure 26), which does not fit into any of the categories described by Manighetti et al. (2001). This fault may be two faults growing into each other, and therefore this profile may be an amalgamation of two fault profile graphs. It is also possible that the profiles are contaminated by a crater that they cross near the middle of their trace. This is less probable because the crater is ~2 km in diameter and an order of magnitude smaller than the width of the dip (in the non-normalized throw-profile graph). If the profile is an amalgamation of two separate fault profile graphs, or if the dip can be discounted for any reason this fault appears to have a similar first-order shape as the left side of graben set 2 (unrestricted).

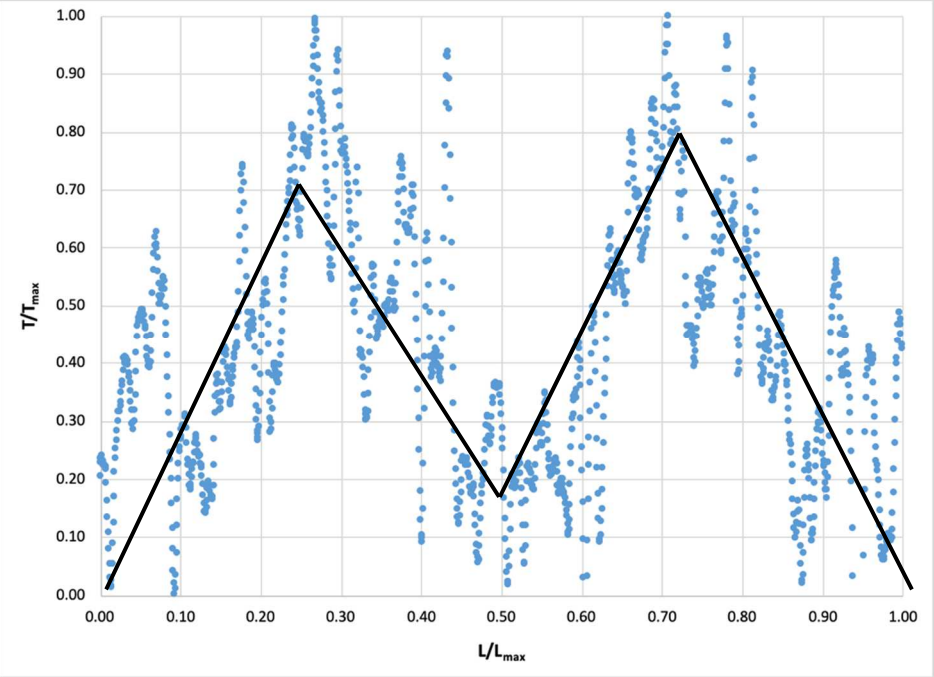

Figure 26: Normalized throw-profile of the right side of graben set 2. Distance between sampled top and bottom profiles was 500 m. Black lines are first-order profile shape which individually fit two unrestricted profiles.

The left side of graben set 3 displays a linear increasing shape on one side, and two different linear profiles on the other side (all marked in black), which is consistent with a tip restricted profile (Figure 27).

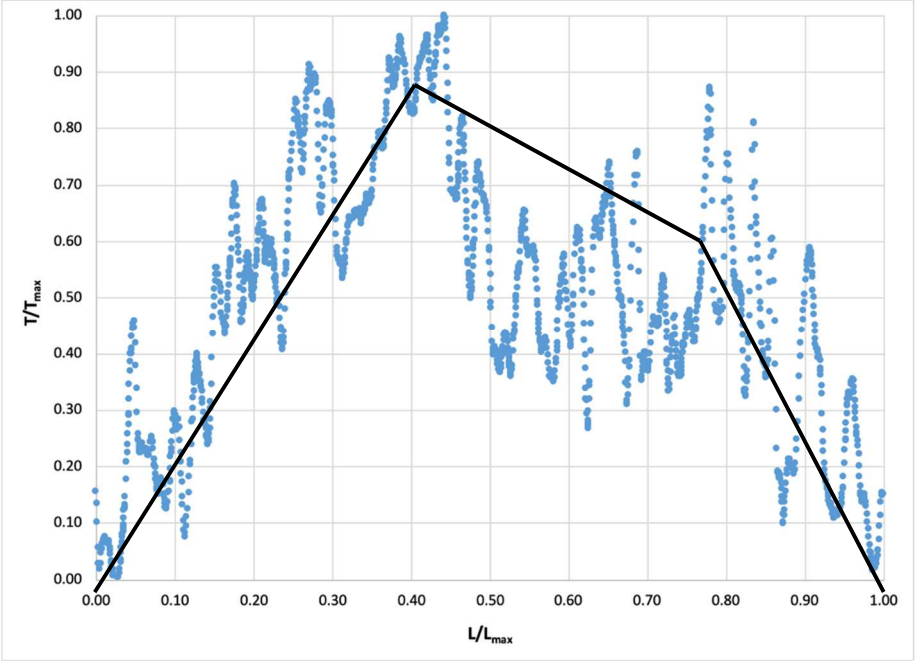

Figure 27: Normalized throw-profile for the left side of graben set 3. Distance between sampled top and bottom profiles was 800 m. Black lines are first-order shape of tip restricted.

The right side of graben set 3 displays an unrestricted slip profile (marked in black), but it is uneven with more slip occurring on one side of the profile than the other (Figure 28). The profile does not bottom out at 0 (T/Tmax or normalized elevation differential), which could be caused by an inaccurate profile length being sampled.

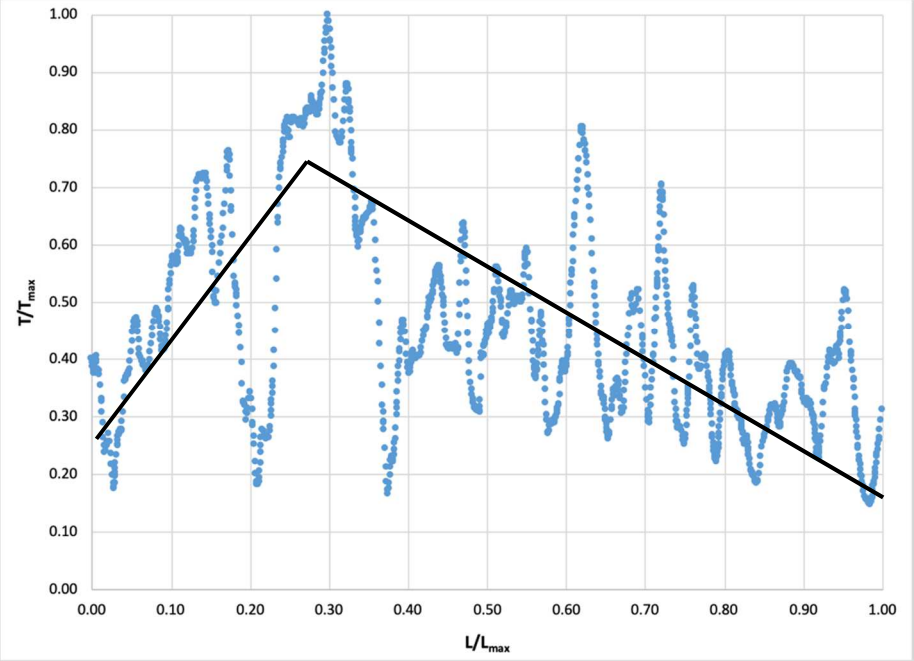

Figure 28: Normalized throw-profile for the right side of graben set 3. Distance between sampled top and bottom profiles was 800 m. First-order shape is unrestricted. Note that there are no values which can be explained by having large differential values even at the edges of the fault trace. This could be accounted for by some of the reasons discussed above and below.

The left profile of graben set 4 appears to have a semi-rounded shape like the quasi-elliptical profiles described in Manighetti et al. (2001) and is classified as such. These occur when there is a boundary to fault propagation and slip continues to occur (Figure 29).

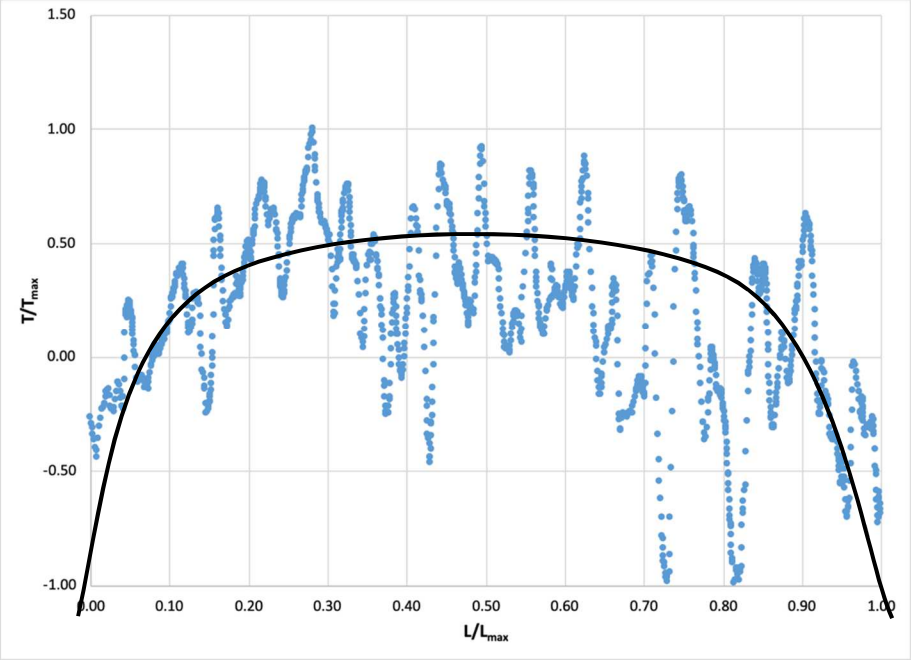

Figure 29: Normalized throw-profile for the left side of graben set 4. Distance between sampled top and bottom profiles was 600 m. First-order shape (black) of quasi-elliptical.

The right profile of graben set 4 has a half-restricted profile where each side is linear but come to a point of maximum displacement not at the middle of the fault (Figure 30). Vertical variation is observed again, which is to be expected because of the limits in the elevation data, as detailed previously.

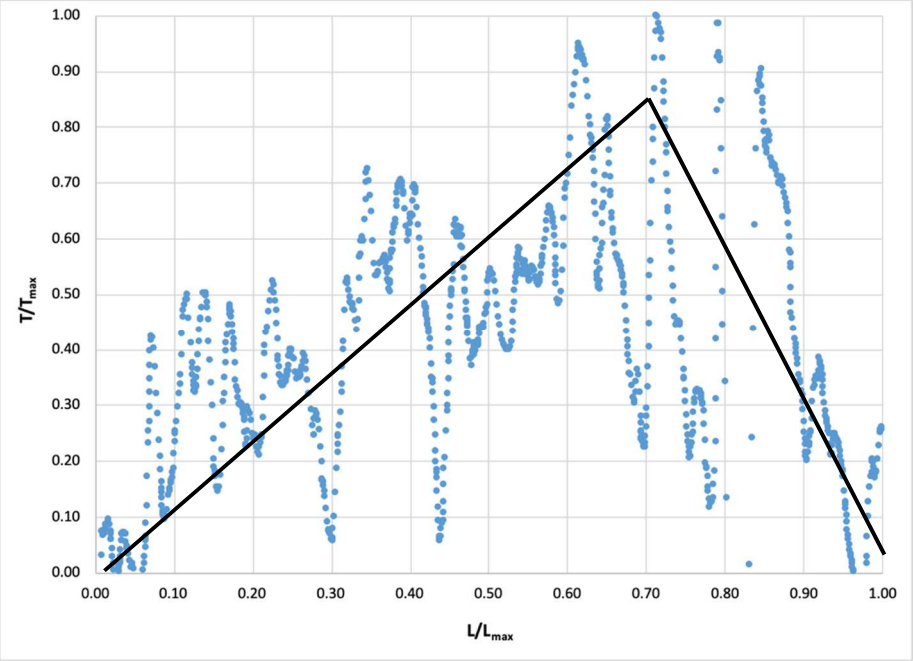

Figure 30: Normalized throw-profile for the right side of graben set 4. Distance between sampled top and bottom profiles was 600 m. First-order shape is unrestricted.

The left of graben set 6 displays an unrestricted profile with two linear limbs which frame a point of maximum displacement (Figure 31). As stated above this indicated a fault which has not reached a barrier to growth.

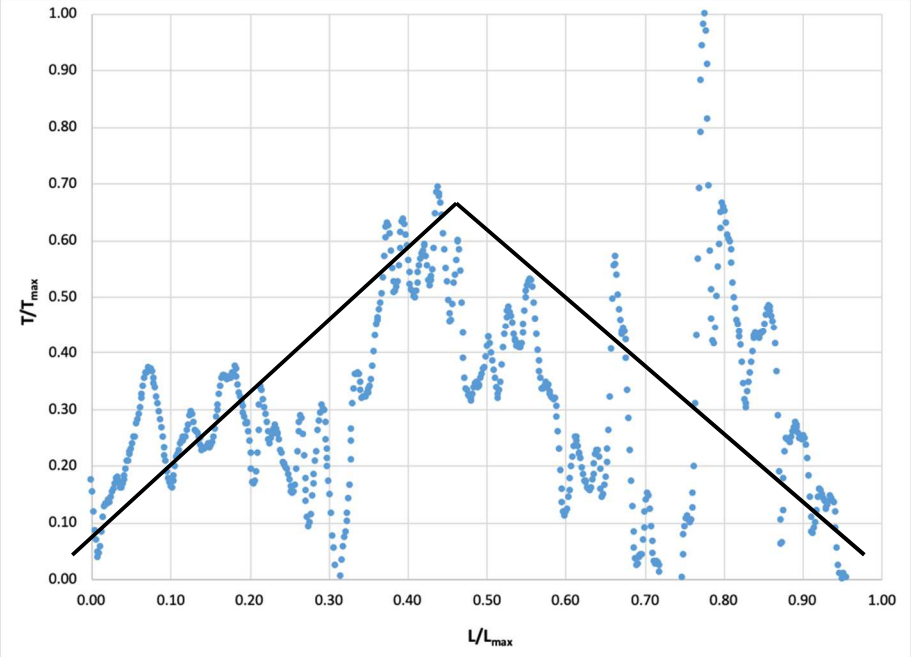

Figure 31: Normalized slip-length profile for the left side of graben set 6. Distance between sampled top and bottom profiles was 800 m. First-order shape is unrestricted.

Because this area is so completely cross cut and stretched by so many faults, we assume that the ground truth fault profiles are more finely detailed than the HRSC DTMs can resolve. Additionally, because all data is derived from optical measurements, there are multiple ways that the profile length may be inaccurate. For example, complete extents of faults may not be traced, or the sample width measured may be too large or too small to capture the profiles accurately. It is also possible that in locations where multiple faults intersect, the traces follow the wrong fault, and should follow a different intersecting fault. Negative (and non-zero such as in Figure 29) elevation values can be explained by only having 10m 3D point certainty, too great of a sample width between the top and bottom profiles of the fault (and therefore crossing other faults in the region and contaminating the sample), or the complexity of the terrain.

These issues could be resolved by in-situ sampling or with higher precision instruments but are not expected to affect the first order shape analysis completed here.

Additionally, this study was designed with limited investigation into the throw-profiles, and thus results are only preliminary and need continued investigation for validation, and no determinations about whole field behavior can be made. The fault growth processes across the region are broadly self-similar, because they share similar slip-length profile shapes (5 unrestricted profiles, 1 tip restricted profile, and 1 quasi-elliptical profile). This indicates that stress fields were consistent.

3.5 SECTOR DIAGRAMS

As described in Chapter 2 sector diagram analysis was utilized to visualize the average orientation direction of the faults in our study area. Figure 32 (a-c) graphically displays the results for normal faults, approximate faults, and approximate normal faults respectively. Faults propagate in NNE and SSW directions predominately across all three sector diagrams. This is indicative of a deformation field which "pulled" in one direction steadily. The approximate fault diagram displays an outlier bin which propagated in an E and W direction. This could be because of misidentification of linear features as faults, or of smaller en echelon tip faults, perpendicular to most faulting, releasing tension and

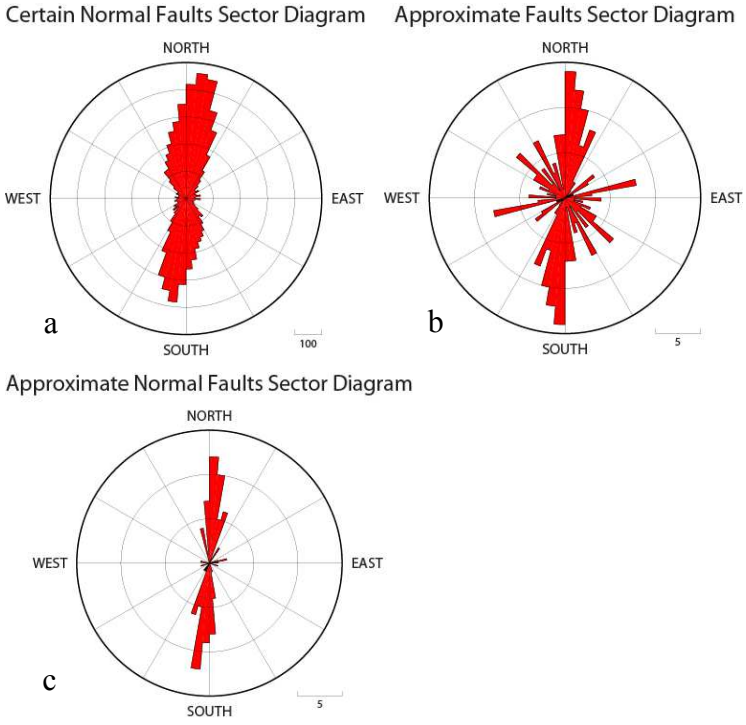

Figure 32: Sector diagrams for normal faults (a), approximate faults (b), and approximate normal faults (c). The normal fault diagram displays a predominately NNE by SSW fault propagation direction. The approximate fault diagram displays mirroring across ± 180° because of azimuth uncertainty and therefore every fault is counted twice, however this does not detract from the pattern of N-S propagation dominance. The approximate normal faults also display a preference for NNE-SSW propagation.

allowing for continued extension in the primary direction of strain. It is worth noting that this method of analysis only looked at numbers of faults and not the length of fault in any direction that could reveal slightly different sector diagrams. However, this is unlikely to make a significant difference because of the order of magnitude difference in average fault propagation direction between the NNE/SSW faults and the other E/W faults.

3.6 CRATER AGE ESTIMATES

Crater age analysis was completed for three sections DH, UL, and LR. Two absolute model ages (AMAs) were estimated for the DH; 3.5 (+0.006, -0.1) and 3.6 (+0.05, -0.07) Ga (Figure 33). The uncertainties on these model ages are the boundaries on the age estimates based on the probability defined in the Poisson fit developed by (Michael and Neukum, 2010) as described in Chapter 2. As shown in Figure 33, part of the crater size frequency distribution (CSFD) falls within one isochron estimate while another part falls within a different isochron estimate. For craters with diameters between 1 and 2 km, the slope of the distribution abruptly changes at an inflection point, which is most likely the result of a resurfacing event. These two age estimates overlap within error, so it is possible that there is only one age for the region. It is more likely there are two ages caused by a resurfacing event given the extensive deformation seen in the DH. Because the area is riddled with faults, the ages determined in this analysis may be the age of emplacement of the original surface and for the resurfacing because of extension. When extension occurs in normal faulting and graben sets, it preferentially destroys craters of a size similar to the average graben width (~a few kms in the DH). This is consistent with crater diameters at which the inflection point is located in the CSFD

occurs, which lends support to this idea. As mentioned in Chapter 2 the UL was not able to resolve an estimated age. The LR however does have an estimated age of 3.6 (+0.06, -0.07) (Figure 34). This area was sampled to estimate an age for the graben sets in the LR section of the DH. However, given that this age is older than the age estimated for the entire DH, it is possible that this age is a background age for the surface before deformation, and not the age of resurfacing. This implies that the DH unit was emplaced and then deformed twice in rapid succession, with emplacement around 3.9 Ga and the two episodes of deformation and extension around 3.6 and 3.5 Ga respectively.

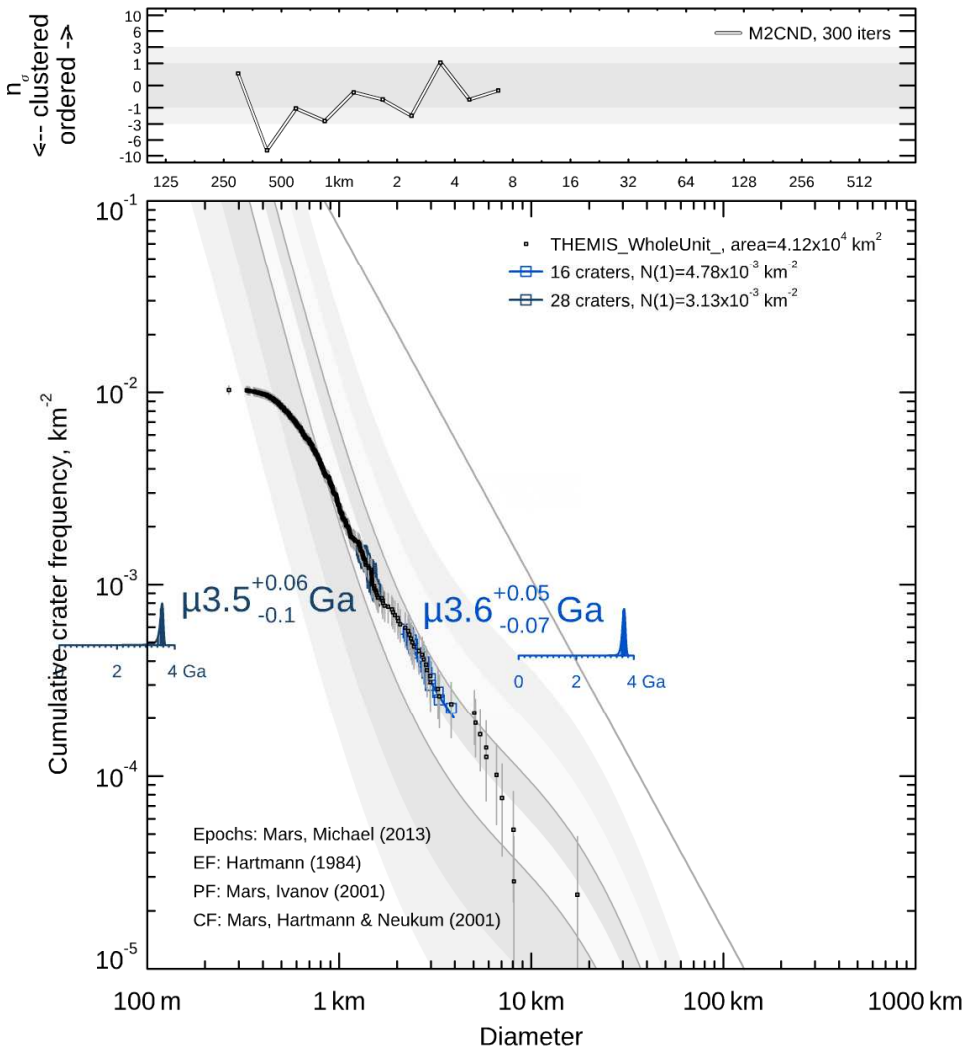

Figure 33: Absolute model ages derived for the Dissected Highlands (DH) via Crater Size Frequency Diagrams (CSFD) generated utilizing CraterStats (Michael and Neukum, 2010). The kink in the crater counts is typically indicative of a resurfacing event and is bounded by two age estimates.

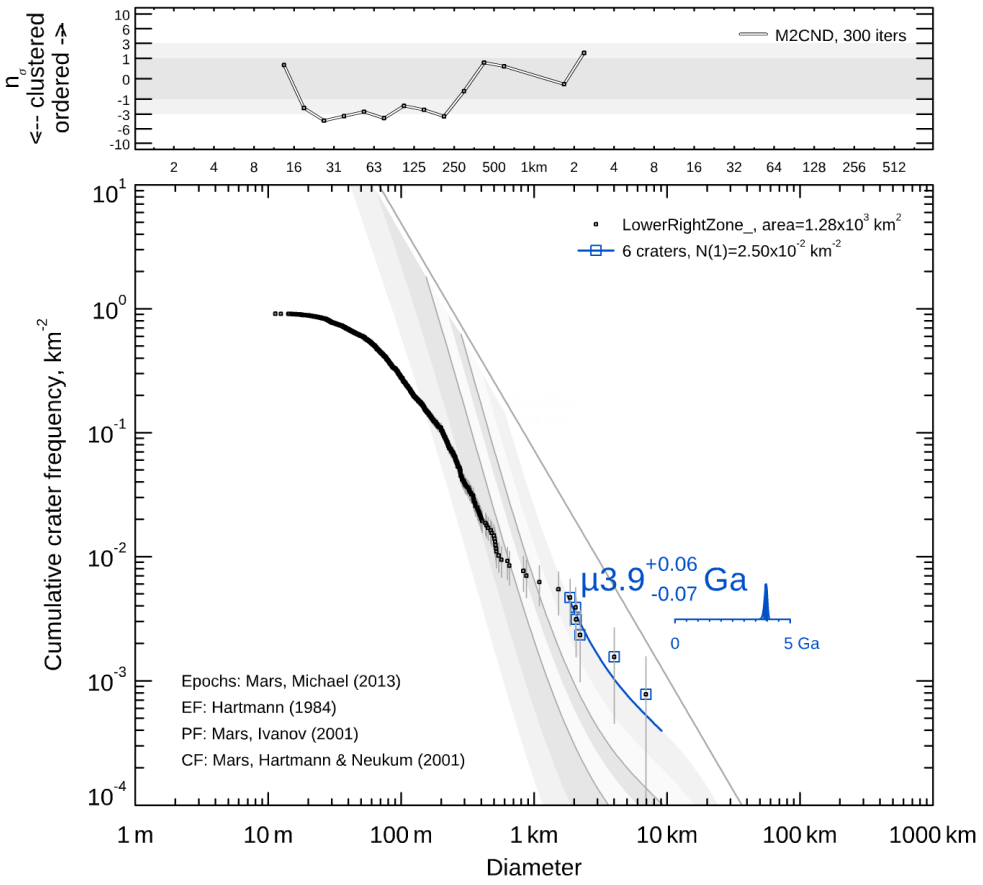

Figure 34: Absolute model age derived for the Lower Right (LR) section, derived via CSFD generated utilizing Craterstats (Michael and Neukum, 2010).

3.7 GEOLOGIC HISTORY

A timeline of events can be determined from this study (Figure 35) by using superposition, crosscutting relationships, surface examination for mapping, and crater age models. First, a surface was emplaced and then modified by extension pulling the surface apart in an east-west direction. Faults grew NNE/SSW. This extension was possibly caused by an intrusion at depth of either a magma chamber or a sub-surface dike swarm and also caused an uplifting of the center of the ROI (if it was an active versus passive rifting zone, discussed in Chapter 4). Then, a second episode of extension occurred, uplifting the northern end of the ROI and causing crosscutting of the LR section of grabens. This extension may have been caused by similar mechanisms as the previous episode of extension. Next, a large graben opened up part of the eastern edge of the uplifted ROI. This graben created a lowland which, along with the eastern side of the ROI, was covered by a layer of volcanic rock (most likely as a lava flow). This lower area in the middle of the large graben and the area to the east were pulled apart some by more extension, but to a lesser extent than the previous extension. The very western edge of the ROI then experienced deposition of volcanic rock.

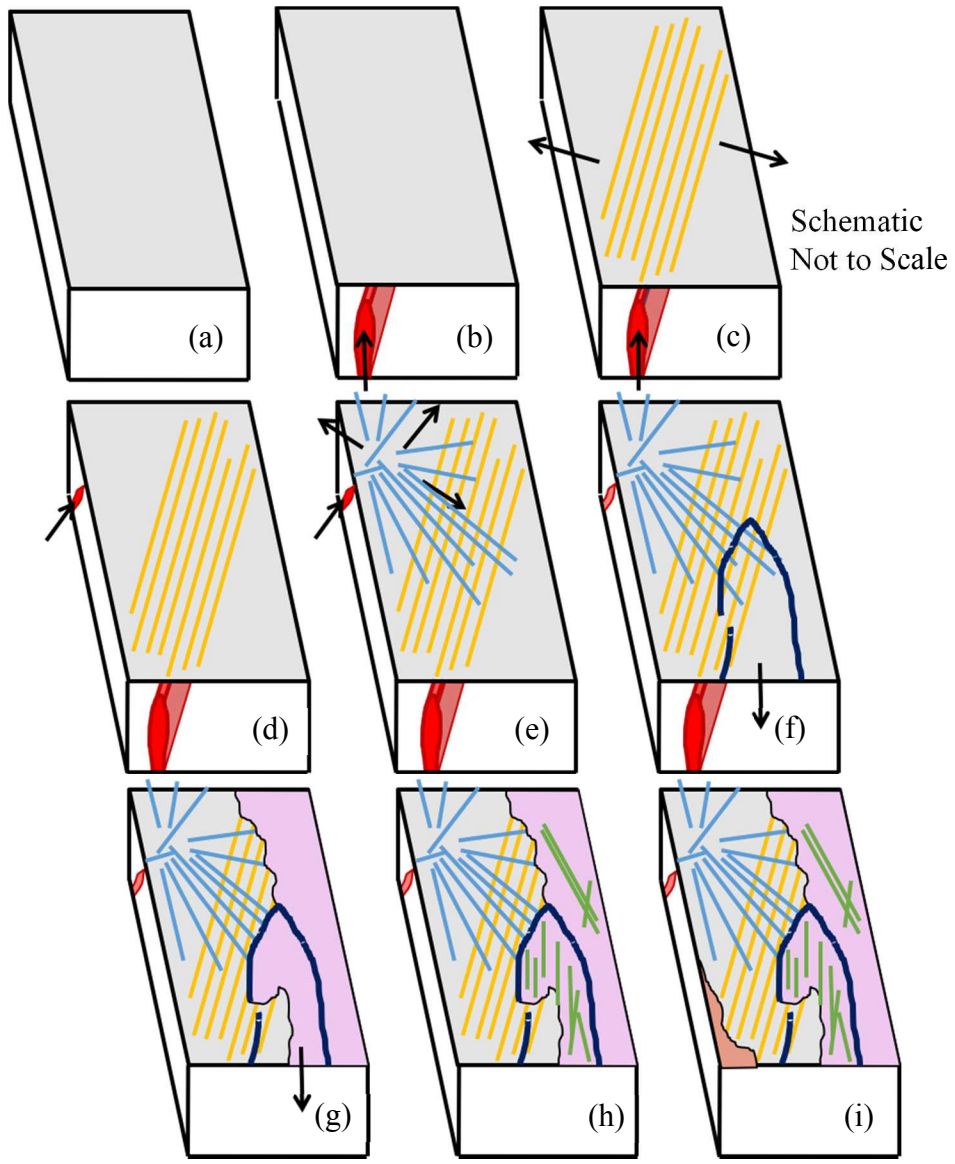

Figure 35: Cartoon of the ROI through time, note that the images are not to scale, and north is up. (a): The original emplaced surface. (b) Intrusion of magma at depth, (c) East-west extension and graben formation caused by (b). (d) New intrusion at depth of magma in the NE corner of the ROI. (e) Uplift above the new intrusion, and extension causing fault and graben propagation across the ROI. (f) Creation of the large Thaumasia graben and down dropping of the middle/inside of the graben. (g) Magma and volcanic rock emplacement along the eastern ROI, continued downward pulling of the middle of the large Thaumasia graben. (h) New extension, graben, and fault production across the youngest volcanics in the ROI. (i) Emplacement of new volcanic on the SW edge of the ROI.

CHAPTER 4

CONCLUSION

This study investigated northern Claritas Fossae and the large Thaumasia graben to assess possible formation mechanisms for geologic features documented here. I investigated three formation mechanisms, a mega-landslide, a rift system, and an underlying dike swarm, as described in Chapter 1. I created a geomorphologic map, a structural feature map, sector diagram analysis of fault propagation, extension and strain analysis across local and regional scales, along strike throw-profile analysis, and absolute model age estimates of locations based of crater counting analysis. This study furthered the work done by Tanaka et al., (2014), and Dhom et al., (2001), in mapping the region. Figures 36 and 37 compare their maps (a) with mine (b). Below I will detail how the results of this study provide support for or refute the formation mechanisms described in Chapter 1, Table 5 summarizes this analysis.

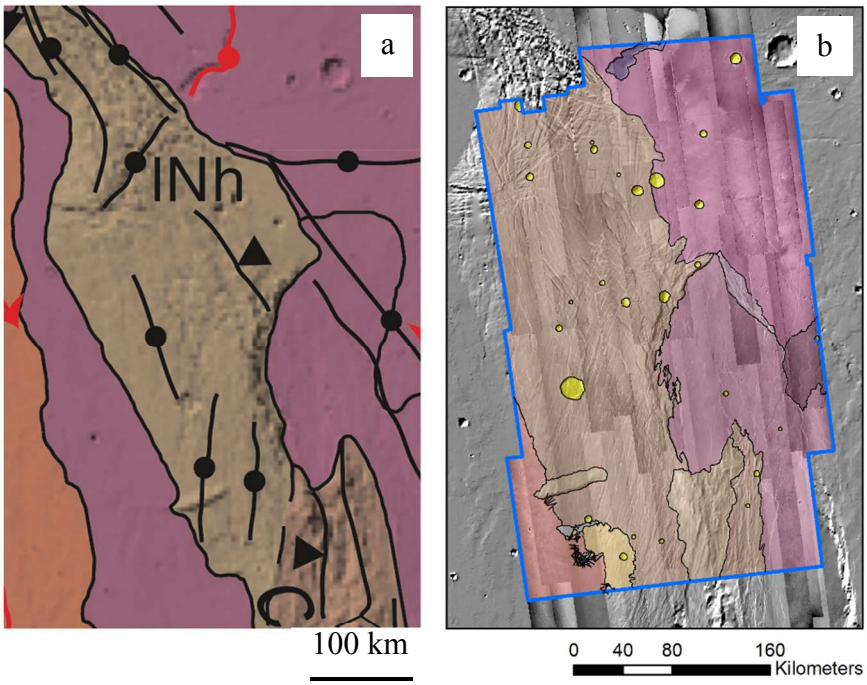

Figure 37: ROI map comparison between (a) the *Geologic Map of Mars* by Tanaka et al. (2014), and (b) my geomorphological map.

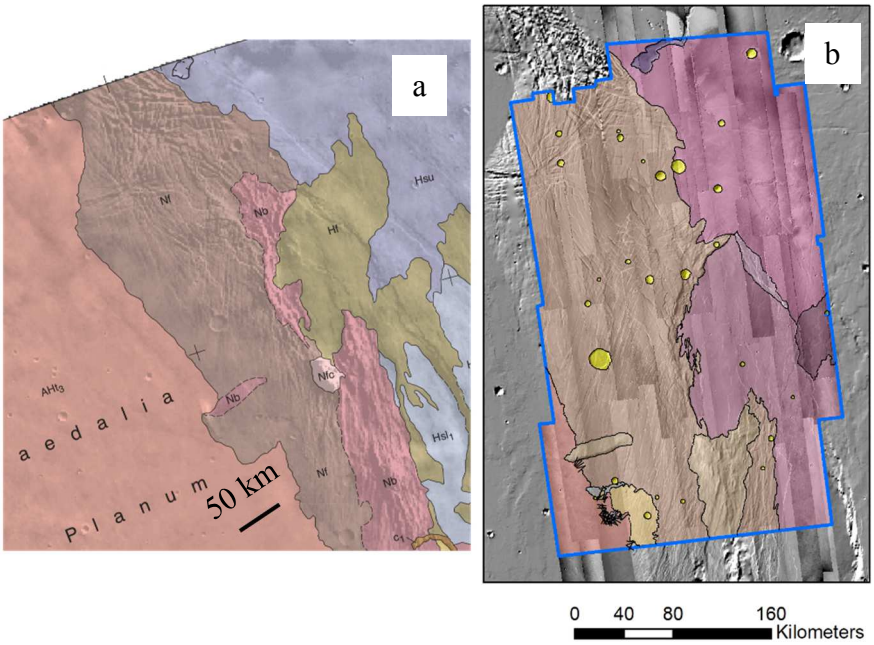

Figure 36: ROI map comparison between (a) the *Geologic Map of the Thaumasia Region, Mars* by Dohm, Tanaka, and Hare (2001), and my (b) geomorphological map.

Table 5: Summary of possible formation mechanisms and evidence thereof.

Formation Mechanism	Key Feature	Evidence of Feature
Mega-landslide*	Rolling Lobate Surface Across Flow	X
	Lobate Edge to Flow with Margin Toe	–
	Scarp Detachment at Origin	–
	Faults Parallel to Flow Front	?
Rift System**	Regional and Locally Uniform Extension	X
	Faulting in Parallel and en echelon Patterns	X
	Faulting in Triple Junction Morphology	X
	Volcanoes and surface lava extents.	–
Underlying Dike Swarm***	Grabens in radiating, circumferential and or subparallel patterns	X
	Pit Craters and Ovoid/Linear Troughs	?
	Spatter Cones and other volcanic features.	–
	Exhumed Dike Outcrops in Graben Centers	?

*Montgomery 2009, and Andrews-Hanna 2009
**Hauber and Kronberg 2005
***Ernst, Grosfils, and Mège 2001
X indicates positive evidence
– indicates lack of evidence
? Indicates circumstantial or uncertain evidence

4.1 Mega-Landslide

Montgomery et al., (2009), and Andrews- Hannah (2009) proposed that the Thaumasia region formed as a mega-landslide. They proposed that the area moved towards the SW as a continent-scale slump, and then compare the region to a terrestrial analog. In this study I found that northern Claritas Fossae has some of the key features expected to be found in a landslide, but not others.

In particular Montgomery et al., identify the left fault of the large Thaumasia graben as a strike-slip fault whereas this study identified the same fault as a normal fault. This line of evidence is described as part of the detachment and scarp near the origin of the mega-landslide in the Montgomery et al., (2009) study. Because I identify the fault as normal and not strike-slip a significant piece of evidence which could have supported the hypothesis put forth by Montgomery et al., (2009) instead refutes it.

It is important to note that I am looking at the equivalent of the top left margin of the proposed continent scale slide and therefore I do not expect to find certain lines of evidence for the slide (specifically lobate edges to the flow front and associated "toe"). Present in my ROI was a rolling lobate surface (as expected for the top of a landslide) on the eastern side of my ROI. I also found some faults parallel to the proposed flow front; however, I also found faults that were not parallel to the flow front. I did not find examples of scarp detachments at the proposed origin point. As mentioned previously I am looking at only a small portion of the proposed mega-landslide and therefore only interpret the evidence supporting the landslide in reference to my ROI.

It is also possible that, because the part of my ROI that corresponds to the flow part of the mega-landslide is covered by relatively young volcanics, that further evidence

to support the mega-landslide hypothesis is covered up. I find that the ROI is similar to the proposed landslide hypothesis in some ways and not in other, it ticks one-and-a-half boxes for evidence in Table 5, and while it cannot be eliminated as a possible formation mechanism this study does not find evidence to strongly support it as a possible mechanism.

4.2 Rift System

Hauber and Kronberg (2005) analyze the Thaumasia graben as a rift system, they analyze the extension of the region and compile a visual geomorphological comparison to the Kenya Rift in Africa on Earth. I find that a better Earth analog for the ROI is the Afar Rift and triple junction in Africa (Figure 38) as it displays similar complex structural relationships to those seen in my study, particularly in the highlighted area (a) which displays geomorphology to similar Figure 17a in Chapter 3. I find that of the features listed in Table 5 for a rift system all, but one is found in my ROI. There is evidence for faulting in parallel to sub-parallel and en echelon graben and fault patterns, regional and locally uniform extension (to a few percentages), and faulting in radiating patterns similar to triple junction morphology. The only feature not present are local volcanoes, or other surface lava expressions associated with and origin acting inside the graben. The results of this study support the possibility of a rift system in Thaumasia and Claritas Fossae.

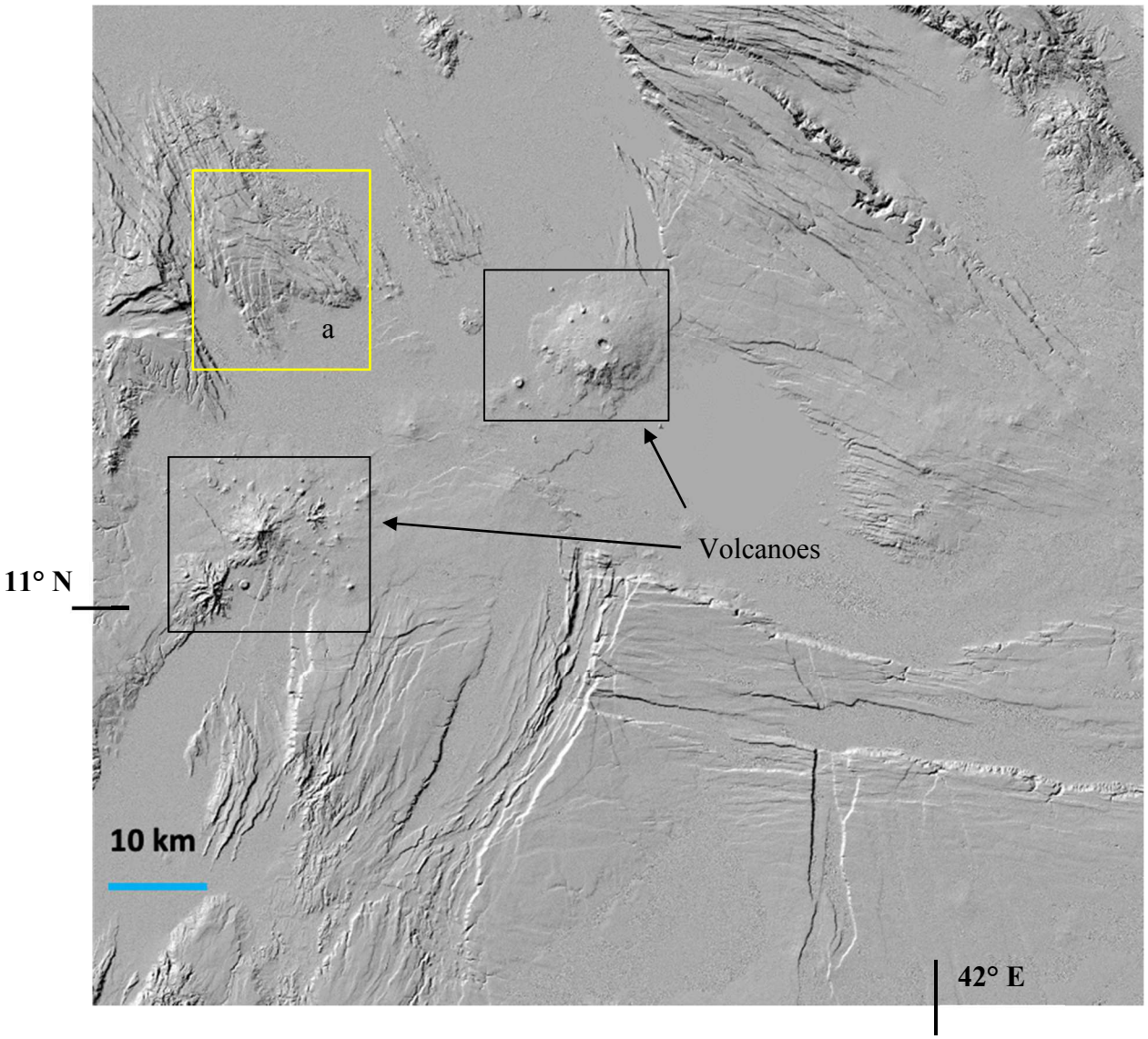

Figure 38: Morphological/structural image of the Afar region on Earth. Output from a 30 m/pixel Shuttle Radar Topography Mission DTM, processed via OpenTopography (Farr et al., 2007). The complex structural relationship between faults in the region including cross cutting fault and graben extensions, as well as the interfingered smoother volcanic plains bear a striking resemblance to the ROI of this study. Box (a) displays a similar morphology to Figure 17b in Chapter 3. There are volcanoes in the Afar triangle which are not present in the ROI.

4.3 Underlying Dike Swarm

Claritas Fossae and Syria Planum are proposed to be giant dike swarms by Ernst, Grosfils, and Mège (2001). They describe surfaces features which can be indicative of sub-surface dikes (summarized and listed in Table 5). This study found that the ROI had several of the features described above including graben sets in radiating and sub-parallel patterns, some pit craters and a possible volcanic collapse feature (ChM described in Chapter 3). The ROI does not contain spatter cones, other volcanoes, or features which can be confidently interpreted as exhumed dikes. There are some linear features at the bottom of some graben sets that might be dikes but the current spatial resolution of the data set, combined with the ubiquitous Martian "dust" layer covering everything means the linear features cannot be identified as dikes with any certainty. Dikes can swarm by themselves but can also swarm above magma chambers during early events of a rift zone initiation, and therefore evidence for this hypothesis can also strengthen the preceding hypothesis of a rift zone. Evidence presented in this study within the ROI both partially supports this hypothesis because of the presence of some criteria for this hypothesis and not others.

4.4 In Summary

Faulting in this study was compared to terrestrial faulting studies by Manighetti et al., (2001) and surface geomorphological investigations were compared to Ernst et al., 2002; Hauber and Kronberg, 2005; and Montgomery et al., 2009.

Figure 35 in Chapter 3 summarizes the sequence of events that are estimated to have occurred in the ROI. The figure displays the complex sequence of events necessary to explain the current surface geomorphology of the ROI.

The sequence is most analogous to what would be present at an initiated but incomplete rift zone, which was then partially covered by surface lava flows. The figure presents an active rift zone, or a zone where uplift occurs due to thermal upwelling (Morgan and Baker, 1983). Regions which undergo active rifting tend to have volcanism which predates rifting, and occur over point sources of magma such as hot spots (Sengör and Burke, 1978). Passive rift zones occur in regions where the crust in thinned and pulled apart by surface tensions and magma upwelling follows (Morgan and Baker, 1983). In the case of passive rifting faulting usually occurs before magmatism, and tends to occur in subparallel patterns (Sengör and Burke, 1978). The two episodes of extension in the ROI occur in two patterns, subparallel and radial. The subparallel pattern occurred first and is more analogous to a passive rift zone formation. The radial pattern is more consistent with an active rift zone formation. However, given that there is little evidence of surface volcanic features in the ROI determining if an active or passive rift zone occurred with either set of extension is not possible, with the current data.

Other studies of faulting on Mars, investigate structural feature identification and quantification specifically, identification of igneous dikes at or near the surface, compressional features, and quantification of displacement-length scaling and strain (Mueller and Golombek, 2004; Polit et al., 2009; Schultz et al., 2010, 2004). This study confined quantitative analysis of faulting to across strike strain, and along strike throw-profile analysis. However, my study does provide insight into regional and local

deformation fields, which are the purpose of most structural studies on Mars. Schultz et al., (2010) describe the need for analysis of structural features on Mars and other planetary bodies to investigate formation processes and causes of surface stress. By analyzing the faulting and extension in the ROI I have developed a story for the region which discusses possible deformation field patterns and formation processes. However, It is my opinion that the actual story is more complex than a single formation mechanism and more in line with the events described in Figure 35 (Chapter 3).

My study is therefore a much-needed addition to the body of work which analyzes faults on Mars.

4.5 Further Work

Further investigation is necessary to refine the exact history of the ROI. Such investigations would include more extension analysis (across a greater number of samples (n), area over which grabens are investigated, and in unit type sampled) and continued along strike throw-profile analysis to determine if trends can be identified on a regional level (specifically to determine if there was a nonuniform deformation field). Analyzing and comparing the values of a more robust dataset for extension/strain analysis and along strike throw-profile analysis to the results of studies completed in the Afar region (particularly those studies completed by Manighetti and others in the lines of Manighetti et al., 2001) would allow us to better compare the two regions.

An expanded set of data for further analysis and extending the analysis both north and south of this ROI would be beneficial. The region could use an increased DTM dataset at the best resolution (50 m/pix from HRSC), or from DTMs derived from CTX

data or another source to produce similar spatial resolution to the visible images for a more direct comparison of CTX (~6 m/pixel) to HRSC DTM (spatial resolution listed above). Additional CTX and or HRSC DTMs would be the most worthwhile data to obtain for the ROI right now, and that HiRISE data has sparse of coverage and the (at this point) excessively fine spatial resolution (~0.3 m/pixel) given the areal extent in this study.

REFERENCES

Anderson, J., Sides, S.C., 2004. Modernization of the integrated software for imagers and spectrometers. Lunar Planet. … 2039.

Andrews-Hanna, J.C., 2009. Planetary science: A mega-landslide on Mars. Nat. Geosci. 2, 248–249. doi:10.1038/ngeo483

Anguita, F., Fernández, C., Cordero, G., Carrasquilla, S., Anguita, J., Núñez, A., Rodríguez, S., García, J., 2006. Evidences for a Noachian-Hesperian orogeny in Mars. Icarus 185, 331–357. doi:10.1016/j.icarus.2006.07.026

Dohm, J. M., Ferris, J.C., Baker, V.R., Anderson, R.C., Hare, T.M., Strom, R.G., Barlow, N.G., Tanaka, K.L., Klemaszewski, J.E., Scott, D.H., 2001. Ancient drainage basin of the Tharsis region, Mars: Potential source for outflow channel systems and putative oceans or paleolakes. J. Geophys. Res. E Planets 106, 32943–32958. doi:10.1029/2000JE001468

Dohm, J.M., Tanaka, K.L., 1999. Geology of the Thaumasia region, Mars: plateau development, valley origins, and magmatic evolution. Planet. Space Sci. 47, 411–431. doi:10.1016/s0032-0633(98)00141-x

Dohm, James M, Tanaka, K.L., Hare, T.M., 2001. Geologic Map of the Thaumasia Region , Mars 80225.

Ernst, R., Grosfils, E., Mège, D., 2002. Giant Dike Swarms: Earth, Venus, and Mars. Annu. Rev. Earth Planet. Sci. 29, 489–534. doi:10.1146/annurev.earth.29.1.489

Grott, M., Hauber, E., Werner, S.C., Kronberg, P., Neukum, G., 2007. Mechanical modeling of thrust faults in the Thaumasia region, Mars, and implications for the Noachian heat flux. Icarus 186, 517–526. doi:10.1016/j.icarus.2006.10.001

Gwinner, K., Scholten, F., Preusker, F., Elgner, S., Roatsch, T., Spiegel, M., Schmidt, R., Oberst, J., Jaumann, R., Heipke, C., 2010. Topography of Mars from global mapping by HRSC high-resolution digital terrain models and orthoimages: Characteristics and performance. Earth Planet. Sci. Lett. 294, 506–519. doi:10.1016/j.epsl.2009.11.007

Hartmann, W.K., Neukum, G., 2001. Cratering chronology and the evolution of Mars. Space Sci. Rev. 96, 165–194. doi:10.1023/A:1011945222010

Hauber, E., Kronberg, P., 2005. The large Thaumasia graben on Mars: Is it a rift? J. Geophys. Res. E Planets 110, 1–13. doi:10.1029/2005JE002407

Hood, D.R., Judice, T., Karunatillake, S., Rogers, D., Dohm, J.M., Susko, D., Carnes, L.K., 2016. Assessing the geologic evolution of Greater Thaumasia, Mars. J.

Geophys. Res. Planets 121, 1753–1769. doi:10.1002/2016JE005046

Ivanov, B.A., 2001. Mars/Moon cratering rate ratio estimates. Space Sci. Rev. 96, 87–104. doi:10.1023/A:1011941121102

Jaumann, R., Neukum, G., Behnke, T., Duxbury, T.C., Eichentopf, K., Flohrer, J., Gasselt, S. v., Giese, B., Gwinner, K., Hauber, E., Hoffmann, H., Hoffmeister, A., Köhler, U., Matz, K.D., McCord, T.B., Mertens, V., Oberst, J., Pischel, R., Reiss, D., Ress, E., Roatsch, T., Saiger, P., Scholten, F., Schwarz, G., Stephan, K., Wählisch, M., 2007. The high-resolution stereo camera (HRSC) experiment on Mars Express: Instrument aspects and experiment conduct from interplanetary cruise through the nominal mission. Planet. Space Sci. 55, 928–952. doi:10.1016/j.pss.2006.12.003

Kneissl, T., Michael, G.G., Platz, T., Walter, S.H.G., 2015. Age determination of linear surface features using the Buffered Crater Counting approach - Case studies of the Sirenum and Fortuna Fossae graben systems on Mars. Icarus 250, 384–394. doi:10.1016/j.icarus.2014.12.008

Kneissl, T., Van Gasselt, S., Neukum, G., 2011. Map-projection-independent crater size-frequency determination in GIS environments - New software tool for ArcGIS. Planet. Space Sci. 59, 1243–1254. doi:10.1016/j.pss.2010.03.015

Malin, M.C., Bell, J.F., Cantor, B.A., Caplinger, M.A., Calvin, W.M., Clancy, R.T., Edgett, K.S., Edwards, L., Haberle, R.M., James, P.B., Lee, S.W., Ravine, M.A., Thomas, P.C., Wolff, M.J., 2007. Context Camera Investigation on board the Mars Reconnaissance Orbiter. J. Geophys. Res. E Planets 112. doi:10.1029/2006JE002808

Manighetti, I., King, G.C.P., Gaudemer, Y., Scholz, C.H., Doubre, C., 2001. Slip accumulation and lateral propagation of active normal faults in Afar. J. Geophys. Res. Solid Earth 106, 13667–13696. doi:10.1029/2000jb900471

McEwen, A.S., Banks, M.E., Baugh, N., Becker, K., Boyd, A., Bergstrom, J.W., Beyer, R. a., Bortolini, E., Bridges, N.T., Byrne, S., Castalia, B., Chuang, F.C., Crumpler, L.S., Daubar, I., Davatzes, A.K., Deardorff, D.G., DeJong, A., Alan Delamere, W., Dobrea, E.N., Dundas, C.M., Eliason, E.M., Espinoza, Y., Fennema, A., Fishbaugh, K.E., Forrester, T., Geissler, P.E., Grant, J. a., Griffes, J.L., Grotzinger, J.P., Gulick, V.C., Hansen, C.J., Herkenhoff, K.E., Heyd, R., Jaeger, W.L., Jones, D., Kanefsky, B., Keszthelyi, L., King, R., Kirk, R.L., Kolb, K.J., Lasco, J., Lefort, A., Leis, R., Lewis, K.W., Martinez-Alonso, S., Mattson, S., McArthur, G., Mellon, M.T., Metz, J.M., Milazzo, M.P., Milliken, R.E., Motazedian, T., Okubo, C.H., Ortiz, A., Philippoff, A.J., Plassmann, J., Polit, A., Russell, P.S., Schaller, C., Searls, M.L., Spriggs, T., Squyres, S.W., Tarr, S., Thomas, N., Thomson, B.J., Tornabene, L.L., Van Houten, C., Verba, C., Weitz, C.M., Wray, J.J., 2010. The High Resolution

Imaging Science Experiment (HiRISE) during MRO's Primary Science Phase (PSP). Icarus 205, 2–37. doi:10.1016/j.icarus.2009.04.023

Michael, G.G., 2013. Planetary surface dating from crater size-frequency distribution measurements: Multiple resurfacing episodes and differential isochron fitting. Icarus 226, 885–890. doi:10.1016/j.icarus.2013.07.004

Michael, G.G., Neukum, G., 2010. Planetary surface dating from crater size-frequency distribution measurements: Partial resurfacing events and statistical age uncertainty. Earth Planet. Sci. Lett. 294, 223–229. doi:10.1016/j.epsl.2009.12.041

Michael, G.G., Platz, T., Kneissl, T., Schmedemann, N., 2012. Planetary surface dating from crater size-frequency distribution measurements: Spatial randomness and clustering. Icarus 218, 169–177. doi:10.1016/j.icarus.2011.11.033

Montgomery, D.R., Gillespie, A., 2005. Formation of Martian outflow channels by catastrophic dewatering of evaporite deposits. Geology 33, 625–628. doi:10.1130/G21270.1

Montgomery, D.R., Som, S.M., Jackson, M.P.A., Schreiber, B.C., Gillespie, A.R., Adams, J.B., 2009. Continental-scale salt tectonics on Mars and the origin of Valles Marineris and associated outflow channels. Bull. Geol. Soc. Am. 121, 117–133. doi:10.1130/B26307.1

Morgan, P., Baker, B.H., 1983. Introduction—processes of continental rifting. Dev. Geotecton. 19, 1–10. doi:10.1016/B978-0-444-42198-2.50007-9

Mueller, K., Golombek, M., 2004. Compressional Structures on Mars. Annu. Rev. Earth Planet. Sci. 32, 435–464. doi:10.1146/annurev.earth.32.101802.120553

Nahm, A.L., Schultz, R.A., 2010. Evaluation of the orogenic belt hypothesis for the formation of the Thaumasia Highlands, Mars. J. Geophys. Res. 115. doi:10.1029/2009je003327

Neukum, G., 1983. Meteorite Bombardment and Dating of Planetary Surfaces 1–186.

Platz, T., Michael, G., Tanaka, K.L., Skinner, J.A., Fortezzo, C.M., 2013. Crater-based dating of geological units on Mars: Methods and application for the new global geological map. Icarus 225, 806–827. doi:10.1016/j.icarus.2013.04.021

Polit, A.T., Schultz, R.A., Soliva, R., 2009. Geometry, displacement-length scaling, and extensional strain of normal faults on Mars with inferences on mechanical stratigraphy of the Martian crust. J. Struct. Geol. 31, 662–673. doi:10.1016/j.jsg.2009.03.016

Schultz, R.A., Hauber, E., Kattenhorn, S.A., Okubo, C.H., Watters, T.R., 2010. Interpretation and analysis of planetary structures. J. Struct. Geol. 32, 855–875. doi:10.1016/j.jsg.2009.09.005

Schultz, R.A., Okubo, C.H., Goudy, C.L., Wilkins, S.J., 2004. Igneous dikes on Mars revealed by Mars Orbiter Laser Altimeter topography. Geology 32, 889–892. doi:10.1130/G20548.1

Sengör, A.M.C., Burke, K., 1978. Relative timing of rifting and volcanism on Earth and its tectonic implications. Geophys. Res. Lett. 5, 419–421. doi:10.1029/GL005i006p00419

Tanaka, K.L., Skinner, J.A., Dohm, J.M., Irwin, R.P., Kolb, E.J., 2014. Pamphlet accompanies map 3292.

Williams, J.P., Nimmo, F., Moore, W.B., Paige, D.A., 2008. The formation of tharsis on mars: What the line-of-sight gravity is telling us. J. Geophys. Res. E Planets 113. doi:10.1029/2007JE003050

APPENDIX A

LISTS OF HRSC AND CTX DATA USED IN THIS STUDY

Table 6: List of HRSC DTMs used in this study.

Product ID	Spacecraft Clock Start Count	Center Latitude
H2109_0000_DT4	1/0073982504.57946	0
H2120_0000_DT4	1/0074248581.57319	0
H2131_0000_DT4	1/0074514659.56189	0
H2153_0001_DT4	1/0075046827.56179	0

Table 7: List of CTX products used in this study. Continued next page.

Product ID	Spatial Summing	Center Latitude	Spacecraft Clock Start Count	Local Time
B01_010002_1596_XI_20S110W	1	-20.5	0905805264:218	15.62
B05_011571_1622_XN_17S106W	1	-17.84	0916368779:168	15.9
B18_016661_1605_XN_19S107W	1	-19.57	0950635919:061	15.05
D04_028832_1584_XN_21S106W	1	-21.61	1032574879:225	15.69
D05_029109_1576_XN_22S108W	1	-22.41	1034439735:072	15.7
D06_029676_1622_XN_17S109W	1	-17.94	1038257258:195	15.61
D07_029821_1560_XN_24S107W	1	-24.04	1039233323:093	15.56
D13_032445_1619_XN_18S109W	1	-18.13	1056900045:244	14.24
D15_033157_1588_XN_21S108W	1	-21.29	1061693777:186	14.51
D16_033302_1571_XN_22S106W	1	-23.01	1062670015:173	14.59
D18_034080_1645_XI_15S108W	1	-15.59	1067907988:233	14.91
D21_035359_1634_XI_16S107W	1	-16.69	1076519140:223	15.33
D22_035847_1606_XN_19S109W	1	-19.56	1079804426:177	15.44
F02_036559_1598_XN_20S106W	1	-20.19	1084597604:203	15.59
F03_036915_1587_XN_21S106W	1	-21.34	1086994617:074	15.65
F03_037126_1536_XI_26S106W	1	-26.48	1088415089:215	15.74
F04_037271_1566_XI_23S106W	1	-23.5	1089391383:222	15.72
F04_037403_1608_XN_19S109W	1	-19.25	1090280080:094	15.76
F05_037693_1631_XN_16S106W	1	-16.93	1092232436:133	15.84
F05_037759_1600_XN_20S107W	1	-20.09	1092676666:019	15.91
F06_038313_1628_XN_17S110W	1	-17.24	1096405804:056	15.81
F07_038392_1635_XI_16S106W	1	-16.58	1096937432:221	15.78
F07_038590_1578_XN_22S108W	1	-22.21	1098269668:117	15.77
F08_039065_1571_XN_22S109W	1	-23.03	1101465977:158	15.51
F09_039210_1622_XN_17S109W	1	-17.83	1102442339:241	15.37
F09_039421_1578_XI_22S110W	1	-22.24	1103862846:209	15.17
F10_039566_1634_XN_16S108W	1	-16.68	1104839087:043	15.04
F10_039711_1601_XI_19S107W	1	-20.02	1105815157:233	14.89

F14_041333_1602_XI_19S108W	1	-19.95	1116734878:213	14.38
F16_042190_1604_XI_19S108W	1	-19.76	1122504933:229	14.63
F18_042691_1634_XN_16S106W	1	-16.62	1125877987:130	14.87
F19_043047_1618_XN_18S106W	1	-18.21	1128274646:071	14.95
G05_020274_1595_XN_20S107W	1	-20.54	0974960183:093	15.72
G16_024309_1576_XN_22S108W	1	-22.5	1002125429:074	14.44
G22_026643_1575_XN_22S108W	1	-22.6	1017838780:175	15.28
G22_026933_1569_XN_23S105W	1	-23.18	1019791081:208	15.33
J05_046779_1617_XN_18S109W	1	-18.36	1153397948:041	15.48
J08_047847_1581_XN_21S108W	1	-21.94	1160588823:248	15.19
K04_054809_1613_XN_18S106W	1	-18.71	1207461583:045	15.47
K04_054875_1636_XN_16S108W	1	-16.42	1207905915:176	15.47
K05_055231_1619_XI_18S107W	1	-18.19	1210302467:207	15.5
K06_055785_1568_XN_23S108W	1	-23.22	1214031639:226	15.57
K07_055996_1652_XN_14S109W	1	-14.9	1215452012:244	15.5
K09_056827_1603_XN_19S109W	1	-19.78	1221045017:051	15.08
K11_057658_1585_XI_21S110W	1	-21.57	1226638063:235	14.39
K11_057803_1652_XI_14S108W	1	-14.84	1227614059:232	14.26
P06_003317_1653_XI_14S108W	1	-14.83	0860795424:227	15.61
P07_003884_1652_XI_14S108W	1	-14.91	0864612670:231	15.28
P10_004873_1637_XN_16S108W	1	-16.38	0871270980:208	14.51
P11_005374_1609_XN_19S106W	1	-19.16	0874643939:204	14.31
P11_005440_1652_XI_14S108W	1	-14.82	0875088373:214	14.27
P13_005941_1651_XI_14S107W	1	-15.03	0878461319:232	14.25
P13_006007_1648_XN_15S108W	1	-15.24	0878905716:220	14.3
P15_006719_1651_XI_14S108W	1	-15.03	0883699690:227	14.56
P15_007009_1604_XN_19S106W	1	-19.67	0885652208:230	14.71
P15_007075_1639_XI_16S108W	1	-16.26	0886096616:231	14.73
P17_007721_1652_XN_14S108W	1	-14.83	0890446608:065	15.03
P18_008011_1650_XN_15S107W	1	-15.03	0892399344:082	15.15
P18_008222_1639_XN_16S109W	1	-16.15	0893820151:192	15.19
P19_008367_1652_XI_14S108W	1	-14.86	0894796617:222	15.26
P20_008723_1639_XN_16S109W	1	-16.02	0897193996:239	15.43

THIS PAGE INTENTIONALLY LEFT BLANK

APPENDIX B

STRAIN CALCULATIONS FOR ALL GRABENS

All tables in this appendix utilize measurements from the graphs in Appendix C and are taken from profiles depicted in Figure 22.

Table 8: Horizontal offset and strain calculations for graben set 1.

Trace	L_f (m)	ΣDvi (m)	Tan(α)*	ΣDei (m)	L_i (m)	strain	e (%)
Northern L	1840	110	1.73	63	1776	0.036	3.6
Northern R	1144	99	1.73	57	1086	0.053	5.3
Southern L	1500	163	1.73	94	1405	0.067	6.7
Southern R	1400	54	1.73	31	1368	0.023	2.3

*α of 60°

Table 9: Horizontal offset and strain calculations for graben set 2.

Trace	L_f (m)	ΣDvi (m)	Tan(α)*	ΣDei (m)	L_i (m)	strain	e (%)
Southern	1597	141	1.73	82	1516	0.054	5.4
Lower Middle	1887	159	1.73	92	1795	0.051	5.1
Middle	2525	202	1.73	117	2409	0.048	4.8
Upper Middle	2658	143	1.73	83	2575	0.032	3.2
Northern	1948	104	1.73	60	1888	0.032	3.2

*α of 60 °

Table 10: Horizontal offset and strain calculations for graben set 3.

Trace	L_f (m)	ΣDvi (m)	Tan(α)*	ΣDei (m)	L_i (m)	strain	e (%)
Northern	5659	436	1.73	252	5407	0.047	4.7
Middle	4115	294	1.73	170	3945	0.043	4.3
Southern	5659	436	1.73	252	5407	0.047	4.7

*α of 60 °

Table 11: Horizontal offset and strain calculations for graben set 4.

Trace	L_f (m)	ΣDvi (m)	Tan(α)*	ΣDei (m)	L_i (m)	strain	e (%)
Southern	2545	102	1.73	59	2486	0.024	2.4
Middle	2707	163	1.73	94	2613	0.036	3.6
Northern	2947	89	1.73	52	2895	0.018	1.8

*α of 60°

Table 12: Horizontal offset and strain calculations for graben set 5.

Trace	L_f (m)	ΣDvi (m)	Tan(α)*	ΣDei (m)	L_i (m)	strain	e (%)
Northern	3233	665	1.73	384	2849	0.135	13.5
Upper Middle	3666	470	1.73	271	3394	0.080	8.0
Lower Middle	4220	340	1.73	196	4024	0.049	4.9
Southern	3083	243	1.73	141	2942	0.048	4.8

*α of 60 °

Table 13: Horizontal offset and strain calculations for graben set 6.

Trace	L_f (m)	ΣDvi (m)	Tan(α)*	ΣDei (m)	L_i (m)	strain	e (%)
Northern	1734	104	1.73	60	1674	0.036	3.6
Upper Middle	1849	94	1.73	54	1794	0.030	3.0
Lower Middle	2267	84	1.73	49	2218	0.022	2.2
Southern	2271	205	1.73	118	2153	0.055	5.5

*α of 60 °

Table 14: Horizontal offset and strain calculations for the large Thaumasia Graben.

Trace	L_f (m)	ΣDvi (m)	Tan(α)*	ΣDei (m)	L_i (m)	strain	e (%)
Northern	103705	1344	1.73	776	102929	0.01	0.8
Middle	112700	2345	1.73	1354	111346	0.01	1.2
Southern	81325	1918	1.73	1107	80217	0.01	1.4

*α of 60 °

THIS PAGE INTENTIONALLY LEFT BLANK

APPENDIX C

ACROSS STRIKE ELEVATION PROFILES

All graphs in this appendix visualize measurements used in the calculations in Appendix B.

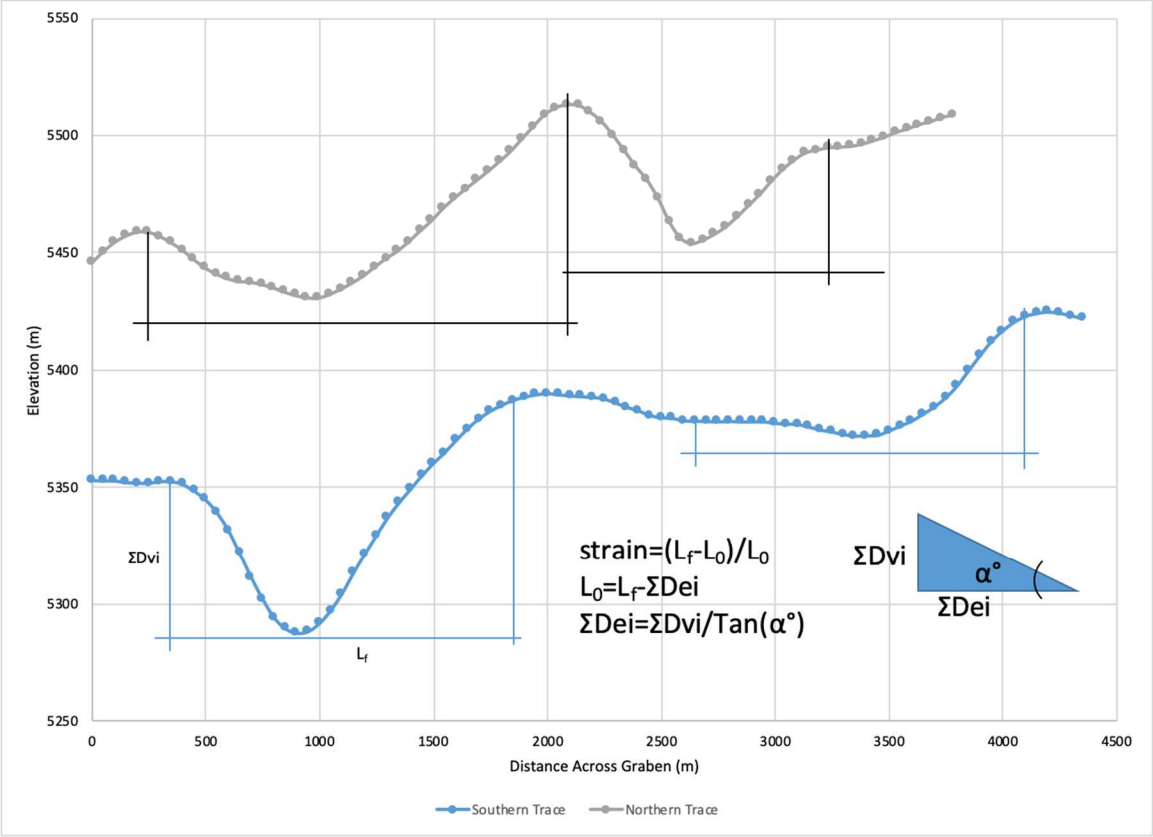

Figure 39: Elevation profiles across graben set 1

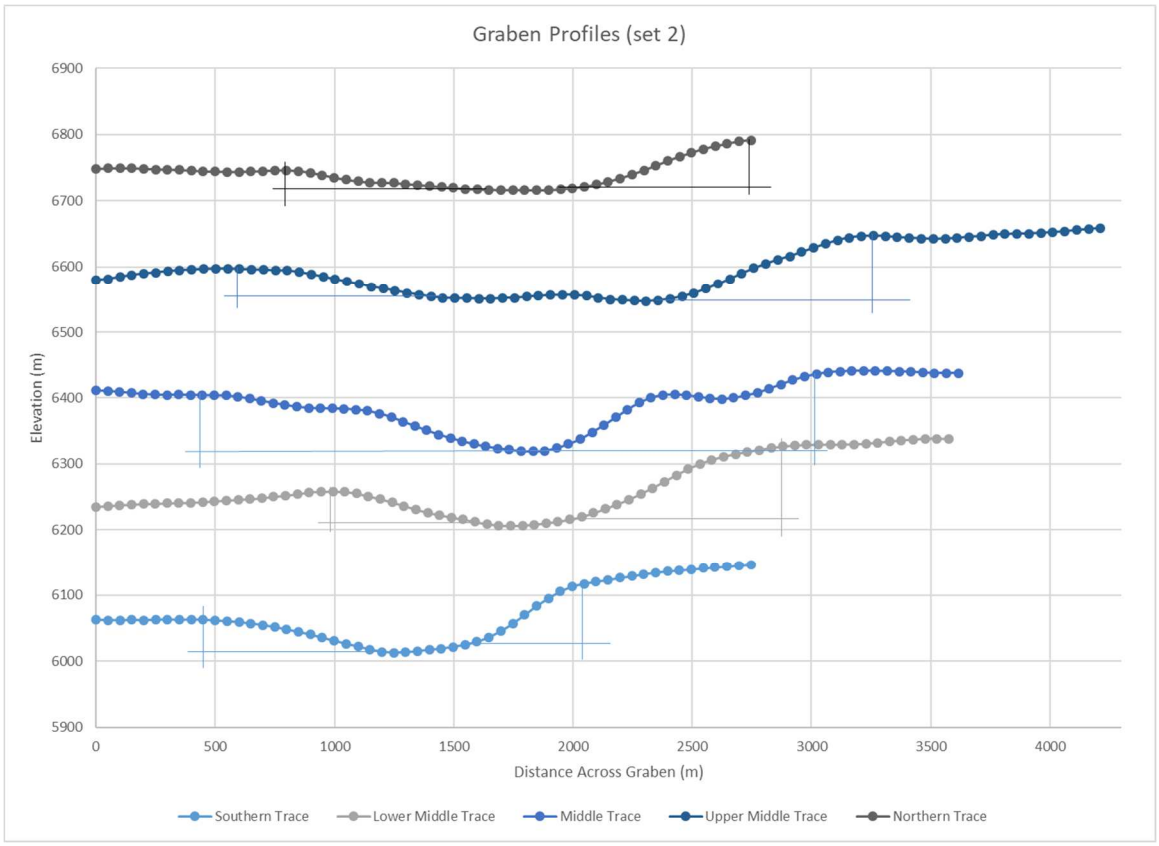

Figure 40: Elevation profiles across graben set 2.

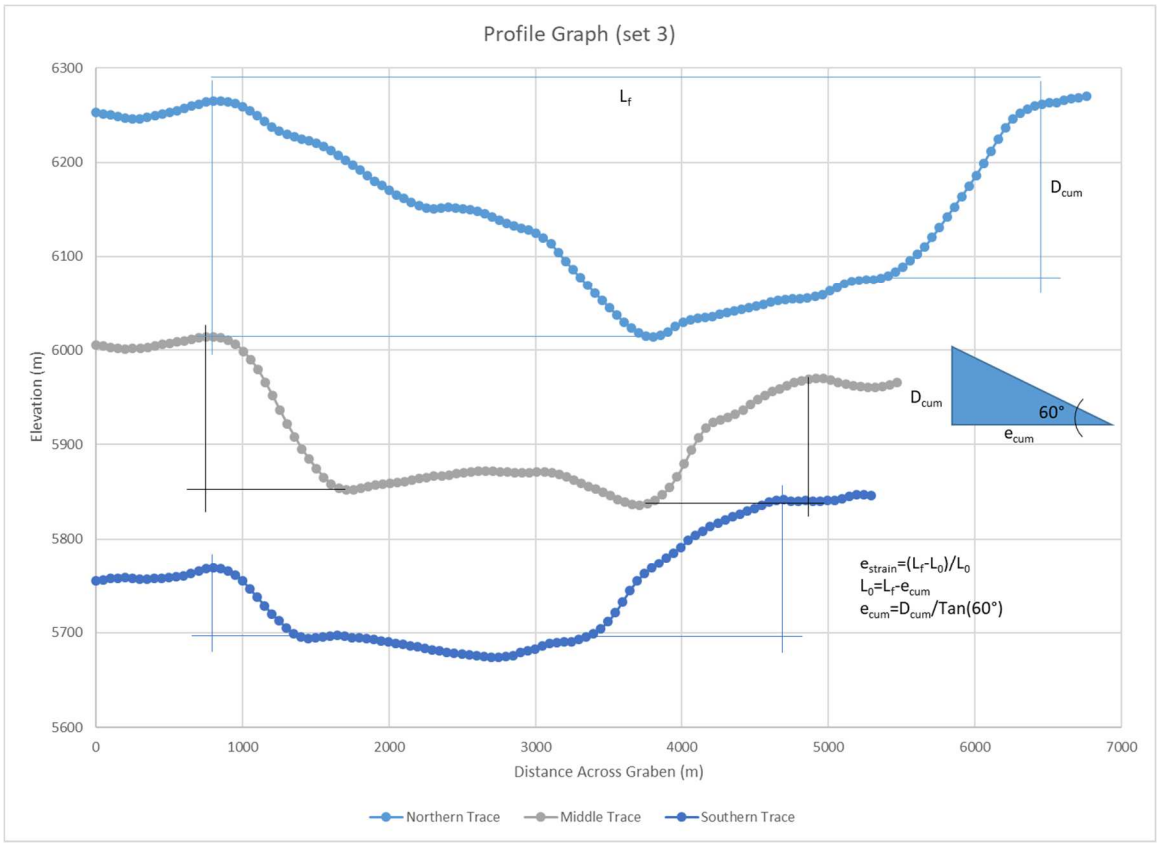

Figure 41: Elevation profiles across graben set 3.

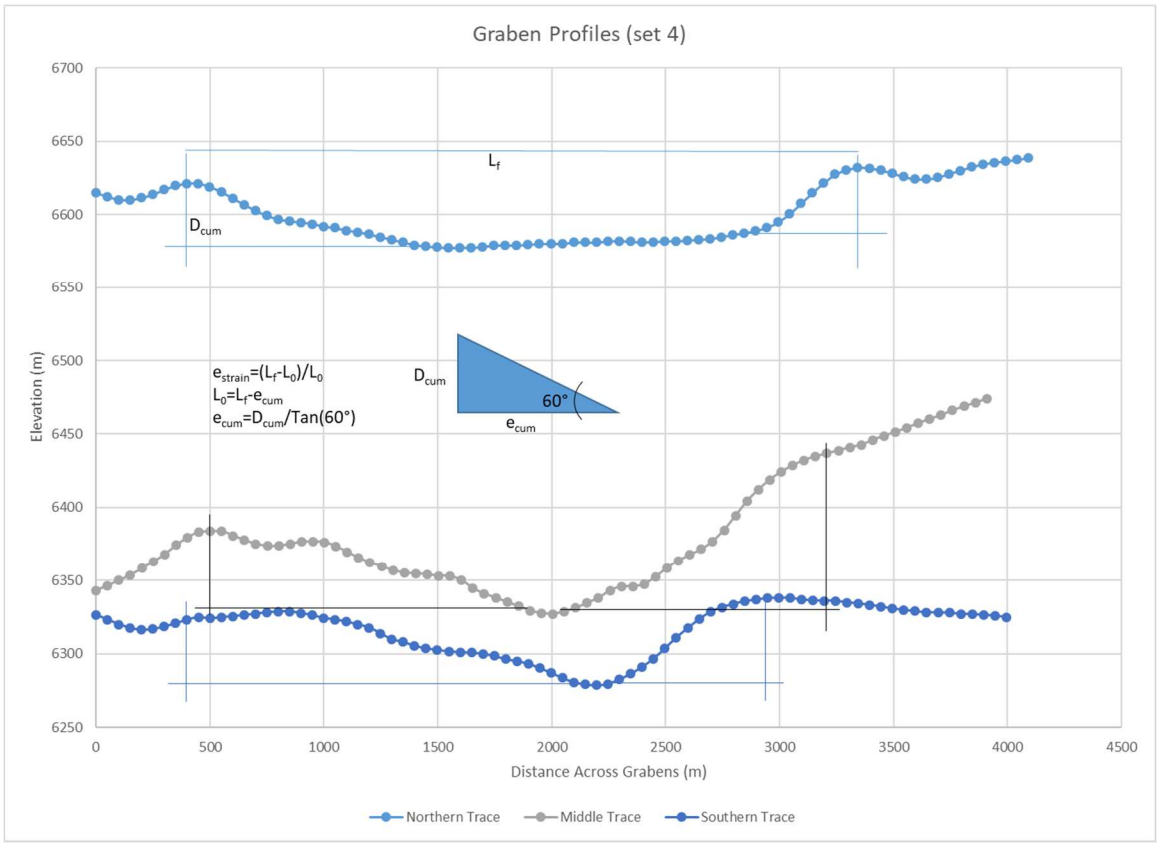

Figure 42: Elevation profiles across graben set 4.

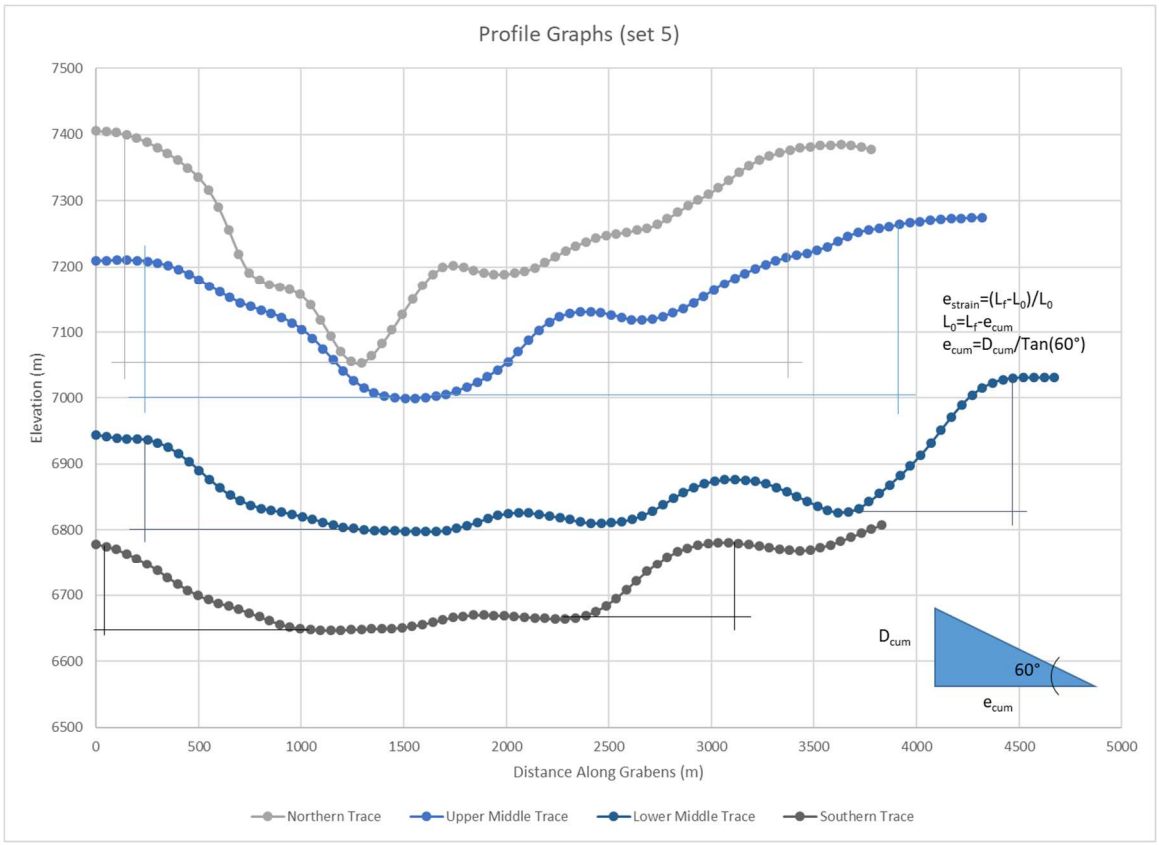

Figure 43: Elevation profiles across graben set 5.

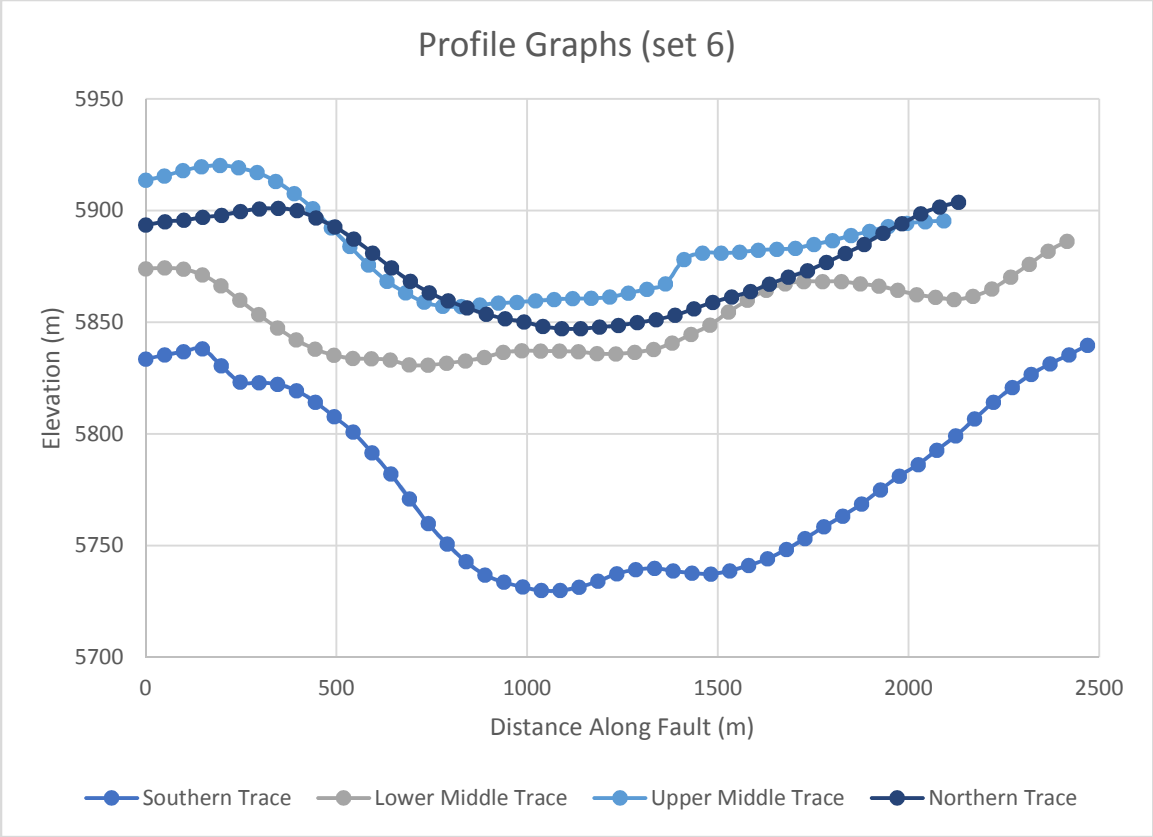

Figure 44: Elevation profiles across graben set 6.

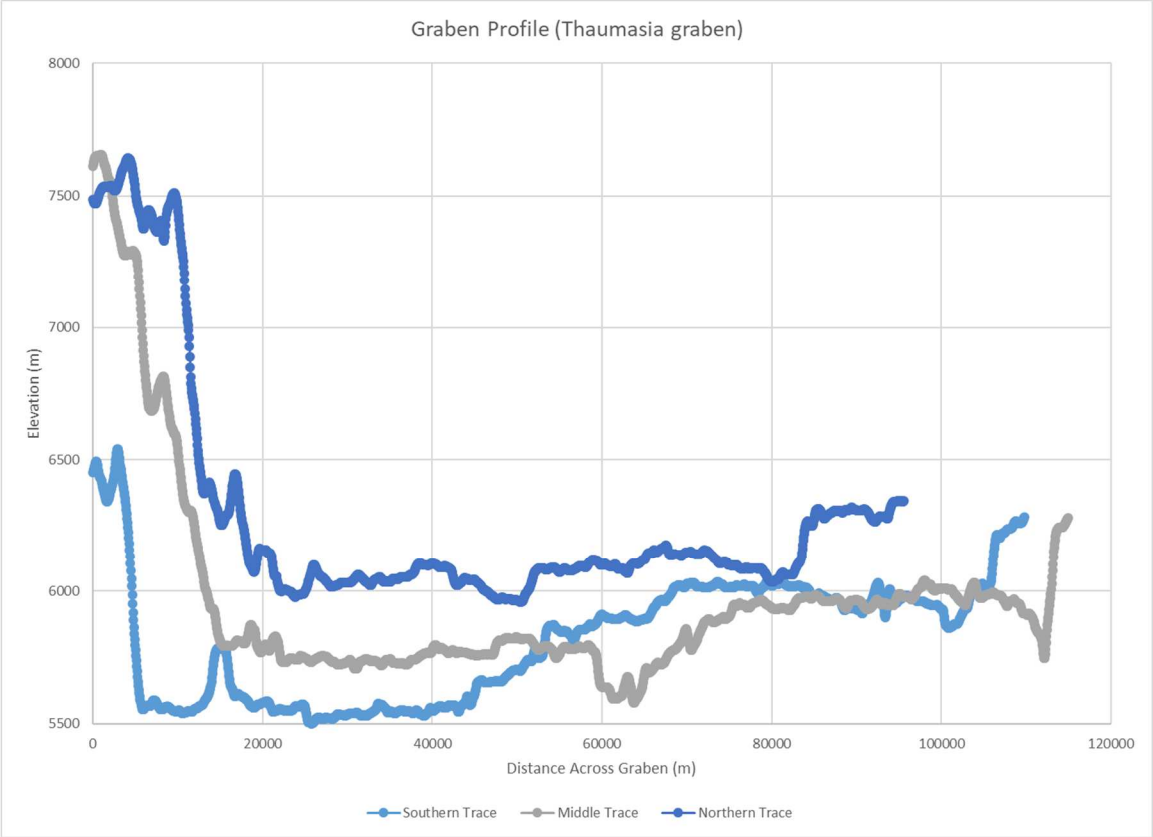

Figure 45: Elevation profiles across the large Thaumasia graben.